

# Assessing the spatial and temporal variability of **MeHg methylmercury** biogeochemistry and bioaccumulation in the Mediterranean Sea with a coupled 3D model

Ginevra Rosati<sup>1</sup>, Donata Canu<sup>1</sup>, Paolo Lazzari<sup>1</sup>, Cosimo Solidoro<sup>1</sup>

5 <sup>1</sup> National Institute of Oceanography and Applied Geophysics - OGS

Correspondence to: Ginevra Rosati (grosati@~~in~~ogs.it)

**Abstract.** Human exposure to mercury (Hg) is a cause of concern, due to the biomagnification of the neurotoxic species monomethylmercury (MMHg) in marine ecosystems. Previous research revealed that commercial fish species in the Mediterranean Sea ecosystems are particularly enriched in Hg, due to a combination of physical and ecological factors. Since  
10 the fate of Hg depends on the interactions among several biogeochemical and physical drivers, biogeochemical modelling is crucial to support the integration and interpretation of field data. Here, we develop and apply a coupled transport-biogeochemical-metal bioaccumulation numerical model (OGSTM-BFM-Hg), to simulate the biogeochemical cycling of the main Hg species (Hg<sup>II</sup>, Hg<sup>0</sup>, MMHg, and DMHg) in seawater, organic detritus, and through the planktonic food web. The model is applied to a 3D domain of the Mediterranean Sea to investigate the spatial and temporal variability of MeHg  
15 distribution and bioaccumulation; ~~and major uncertainties in Hg cycling~~. Model results reproduce the strong vertical and zonal gradients of MeHg concentrations related to primary production consistently with the ~~observations, and~~ [observations and](#) highlight the role of winter deep convection and summer water stratification in shaping the MeHg vertical distribution, including sub-surface MeHg maximum. The modelled bioaccumulation dynamics in plankton food webs are characterized by a high spatial and temporal variability that is driven by plankton ~~phenology, and~~ [phenology and are in agreement with](#) [consistent](#)  
20 with available field data of [Hg](#) concentrations in plankton, ~~as well as~~ [and](#) with other indicators, such as bioconcentration factors (BCFs) and trophic magnification factors (TMFs). Model results pointed out that the increment in water temperature linked to a decline of deep convection can cause an increase in water MeHg concentrations with cascading effects on plankton exposure and bioaccumulation.

## 1 Introduction

25 The anthropogenic alteration of mercury (Hg) biogeochemical cycle has led to global enrichment of Hg concentrations in all the environmental compartments (Amos et al., 2015; UNEP, 2019; Zhang et al., 2014a, 2014b) and concerns over human exposure to neurotoxic monomethylmercury (MMHg), which is produced in the ocean and biomagnifies in marine food webs (UNEP, 2019). The ocean has absorbed 50% of anthropogenic Hg historical emissions, 35% of which ~~are~~ [are](#) currently stored in

the water and the rest in the sediments (Zhang et al., 2014b): relative to pre-anthropogenic levels, the Hg enrichment is 230% in surface ocean waters, 25% in intermediate waters, and 12% in deep waters (UN Environment 2019).

Models and observations (Lamborg et al., 2014; Zhang et al., 2014b) suggest that the oceanic water column contains 280-370 Mmol of anthropogenic Hg (equivalent to about 70000 tons), a large part of which is recycled within surface and intermediate water due to the biological carbon pump and the microbial loop (e.g. Zhang et al., 2018). Hg is scavenged from surface water by organic particles through adsorption and uptake, transported downward via particles sinking, and released in the dissolved phase following particles degradation. The locally increased microbial activity and availability of inorganic Hg at the depth of particles remineralization are also thought to promote Hg methylation (Cossa et al., 2009; Heimbürger et al., 2010; Sunderland et al., 2009). Concurrent biological and photochemical transformations occur in the water column driving the interconversions among the main mercury species in seawater (inorganic oxidized Hg [ $\text{Hg}^{\text{II}}$ ], methylmercury [MMHg], elemental Hg [ $\text{Hg}^0$ ], and dimethylmercury [DMHg]). [Other important processes driving a fast cycling of Hg species in surface water are the atmospheric deposition of oxidized Hg and the gaseous exchange of  \$\text{Hg}^0\$  \(Jiskra et al., 2021\).](#) The resulting vertical distribution of Hg species mirrors the local equilibrium among a number of biogeochemical and physical drivers. However, recent comprehensive reviews of the current understanding of Hg fate in the ocean ([Bowman et al., 2020; Mason et al., 2012; Sonke et al., 2013](#)) and in the Mediterranean Sea ([Cossa et al., 2022](#)) highlighted still high uncertainty in describing and quantifying most of these processes.

MeHg (defined as the sum of MMHg and DMHg) is more frequently measured than the individual methylated species. In oceanic and Mediterranean areas with high primary production, the MeHg vertical distribution is characterized by low concentrations at the surface due to photo-degradation and concentrations maxima coincident with the maximum in apparent oxygen utilization, a proxy for heterotrophic activity (Cossa et al., 2009; Sunderland et al., 2009). These observations suggest that most oceanic MeHg is produced in situ. This conclusion is also supported by estimates of MeHg fluxes in the ocean (Mason et al., 2012; Zhang et al., 2020) and by studies based on stable Hg isotopes (Blum et al., 2013; Motta et al., 2019). The role of DMHg in controlling MMHg dynamics remains puzzling: recent observations (Cossa et al., 2017) from the North Western Mediterranean Sea support the idea that DMHg is produced from  $\text{Hg}^{\text{II}}$  in highly productive waters and then degraded to MMHg (Conaway et al., 2009). However, only an abiotic pathway has been directly identified for the formation of DMHg (Jonsson et al., 2016) and rates of DMHg formation from  $\text{Hg}^{\text{II}}$  measured in polar water were negligible compared to methylation rates from  $\text{Hg}^{\text{II}}$  to MMHg (Lehnherr et al., 2011).

Tunas and other commercial fish species from the Mediterranean Sea are particularly enriched in Hg [in comparison](#) to the same species from other geographical areas (Cossa et al., 2012; Cossa and Coquery, 2005; Harmelin-Vivien et al., 2009; Tseng et al., 2021). It has been suggested that, along with other ecological features of the whole food web, this is due to a shallower occurrence of the MeHg concentrations maxima compared to the Ocean [which](#) results in higher phytoplankton exposure and bioaccumulation (Cossa et al., 2012). Available observations on MeHg distribution in the [Mediterranean](#) Sea suggest that concentrations are lower in the oligotrophic waters of the Ionian Sea than in the mesotrophic waters of the Northwestern Mediterranean (Cossa et al., [2022, 2009](#)) and Adriatic Sea (Kotnik et al., 2015).

Recent efforts to couple the dynamics of biological carbon pump and microbial loop with Hg dynamics, including  
65 bioaccumulation in the lower food web provided global-scale assessments of MeHg production and bioaccumulation (Wu et  
al., 2021, 2020; Zhang et al., 2020). The only study modelling the Hg dynamics in the Mediterranean Sea (Žagar et al., 2007)  
did not include any biological component. Much of the current knowledge on the dynamics of MeHg in the open sea has been  
acquired only afterwards (Bowman et al., 2016, 2015; Cossa et al., 2017, 2009; Heimbürger et al., 2010; Lehnher et al., 2011;  
Monperrus et al., 2007; Munson et al., 2018, 2015; Ortiz et al., 2015; Sunderland et al., 2009).

70 Here, we couple a model for Hg biogeochemistry (Canu et al., 2019; Rosati et al., 2020, 2018; Zhang et al., 2020) with the 3D  
transport biogeochemical model OGSTM-BFM (Cossarini et al., 2021; Lazzari et al., 2021, 2010; Salon et al., 2019) to  
investigate spatial and temporal variability of MeHg dynamics in the Mediterranean Sea. The coupled model, which  
has a 1/16° horizontal resolution, describes the biotic and abiotic interconversions among four Hg species (Hg<sup>II</sup>, MMHg, Hg<sup>0</sup>,  
and DMHg), as well as other key processes of the Hg cycle such as partitioning to [organic](#) detritus, sinking to the seabed,  
75 exchange of gaseous Hg with the atmosphere, and bioaccumulation in 4 phyto- and 4 zooplankton functional groups (Lazzari  
et al., 2012; Vichi et al., 2015). The agreement with observations has been improved by tuning the sinking velocity of organic  
detritus and by exploring the sensitivity to alternative parameterizations of Hg methylation. [A first assessment of the  
uncertainties concerning the fate of riverine Hg loads is also achieved and discussed along with other terms of the Hg budget  
in the Mediterranean Sea.](#) Model results are compared to available observations discussing the implications of spatial and  
80 temporal variability of modelled MeHg distributions in water and plankton.

## 2 Methods

### 2.1 Study area

The Mediterranean Sea (Fig. 1) is a semi-enclosed basin characterized by decreasing west-east gradient of primary production  
resulting from the superposition of biological pump and inverse estuarine circulation, as well as from the limited impact of  
85 riverine loads on the open ocean dynamics (Crise et al., 1999, Crispi et al., 2001). Due to the formation of intermediate and  
deep water generating thermohaline circulation, the Mediterranean is considered a miniature of the ocean  
(Pinardi et al., 2019). The large-scale basin circulation (Pinardi et al., 2019, 2015, Pinardi and Masetti, 2000, and  
references therein) is composed of three thermohaline cells (Fig. 1). A zonal vertical circulation belt is associated with the  
inflow of shallow Atlantic Water (AW) at the Gibraltar Strait that becomes progressively saltier due to evaporation moving  
90 eastward (MAW, Modified Atlantic Water) and eventually sinks at intermediate depths forming the Levantine Intermediate  
Water (LIW), outflowing at Gibraltar. The other cells are driven by dense water formation due to winter  
cooling, salting, and sinking of surface water. Western Mediterranean Deep Water (WMDW) originates in the Northern  
Western Mediterranean Sea, while Eastern Mediterranean Deep Water (EDMW) is formed in the Adriatic Sea, but also in the  
Aegean and the Levantine Sea. The mixing between these deep water masses is inhibited by the shallowness of the Sicily Strait

95 (about 500 m). Long-term observations of ocean colour (Bosc et al., 2004, Bricaud et al., 2002, D’Ortenzio and D’Alcalá,  
2009) and coupled transport-biogeochemical models (Di Biagio et al., 2021, 2019; Lazzari et al., 2021, 2014, 2012) supported  
100 the characterization of different biogeoprovinces based on the seasonal, inter-annual, and high-frequency variability of  
biogeochemical processes in different areas (subbasins). Biogeochemical modelling also revealed the importance of  
subsurface plankton blooms, not captured by ocean colour satellite observations, highlighting the existence of a deep  
chlorophyll maximum that becomes deeper with increasing water oligotrophy. The most productive areas are the mesotrophic  
western subbasins of the Alboran Sea (*Alb*), Northern, and Southern Western Mediterranean (*Nwm* and *Swm*). The eastern  
Mediterranean is ultra-oligotrophic, apart from the Northern Adriatic Sea (*Nad*) which is a coastal  
105 sea, and other “intermittently blooming” areas (i.e., with high inter-annual variability) such as the Southern Adriatic Sea (*Sad*),  
the Aegean Sea (*Aeg*), and the Rhodes Gyre in the Levantine Sea (*Lev*).

## 2.2 The coupled model

The Biogeochemical Flux Model BFM (Vichi et al., 2015) is a model that simulates the cycling of Carbon, Nitrogen  
Phosphorus, and Silica through dissolved, living, and non-living particulate phases of the marine environment. The  
description of the planktonic food web is based on the plankton functional type (PFT) approach: the pool of species having  
110 similar traits (nutrients affinities, light affinity, prey-predator relationships) are described by a  
single variable. In the BFM, PFTs have variable stoichiometry and simulate the lower trophic levels of marine food  
webs up to carnivorous zooplankton (Sect. 2.2.1). The OGSTM-BFM model has been coupled off-line to the ocean general  
circulation model (NEMO) to investigate different issues related to the Mediterranean biogeochemistry (Canu et al., 2015;  
Cossarini et al., 2021, 2015; Lazzari et al., 2021, 2016, 2014, 2012) and it is now routinely used as the backbone of the  
115 biogeochemical component of the Copernicus CMEMS Mediterranean system  
(https://resources.marine.copernicus.eu/products, Salon et al., 2019; Terzić et al., 2019). The integration of a Hg cycling  
module in the BFM-OGSTM model adds more flexibility to this system and opens the way to novel operational oceanography  
applications. Here the OGSTM-BFM-Hg model is implemented (Fig. 2), by coupling the OGSTM-BFM model with the  
equations describing mercury (Hg) species partitioning, transformation, transport (Sect. 2.2.2), bioconcentration in  
120 phytoplankton (Sect. 2.2.3), and trophic transfer to zooplankton (Sect. 2.2.4). The coupled model is used to investigate the Hg  
cycling and bioaccumulation dynamics (Sect. 2.2.5) at the base of the Mediterranean Sea food webs. The model has a 1/16°  
horizontal resolution (approximately 6 km) and 72 vertical levels and runs with a 300 seconds time step. A model spin-up of  
13 years forced with climatological data (Sect. 2.2.6) is performed, and the results of the last year of simulation (2017) are  
analysed.

ha formattato: Tipo di carattere: Corsivo

ha formattato: Tipo di carattere: Corsivo

ha formattato: Tipo di carattere: Corsivo

ha formattato: Tipo di carattere: Corsivo

ha formattato: Tipo di carattere: Corsivo

ha formattato: Tipo di carattere: Corsivo

ha formattato: Tipo di carattere: Corsivo

### 2.2.1 BFM model dynamics

The BFM model dynamically simulates 9 plankton functional types (PFTs) representative of 4 phytoplankton groups (picophytoplankton, nanophytoflagellates, diatoms, and large phytoplankton), 4 zooplankton groups (heterotrophic nanoflagellates, microzooplankton, omnivorous mesozooplankton, and carnivorous mesozooplankton), and 1 group of heterotrophic bacteria (Vichi et al. 2015). The model reproduces the fluxes of carbon, nitrogen, phosphorous, and silicates from the inorganic nutrients pool to organisms (phytoplankton, zooplankton, and bacteria) and organic compounds pools (particulate and dissolved organic carbon, POC<sub>2</sub> and DOC) with a variable stoichiometric formulation. Non-living organic matter includes one class of organic detritus (POC) and three classes of DOC (labile, semi-labile, and semi-refractory).

### 2.2.2 Biogeochemical dynamics in the Hg model

The Hg biogeochemical model (Canu and Rosati, 2017; Canu et al., 2019; Melaku Canu et al., 2015; Rosati et al., 2020, 2018, in prep., Zhang et al., 2020) simulates the cycling of four mercury species in marine water (Fig. 3): inorganic divalent Hg (Hg<sup>II</sup>), monomethylmercury (MMHg), elemental mercury (Hg<sup>0</sup>), and dimethylmercury (DMHg). Eq. (1-4) describe the time variation of non-conservative tracers representing Hg species, omitting advective and diffusive processes that are resolved by the transport model.

$$\frac{d Hg^{II}}{dt} = -k_{met}\{Hg^{II}\} + k_{demet}\{MMHg\} - (k_{phred} + k_{biored})\{Hg_{DOC}^{II} + HgCl_n\} + (k_{phox} + k_{biox})\{Hg^0\} + k_{phdm}(1-\alpha)\{MMHg_{DOC} + MeHgCl\} - \omega_s\{Hg_{POC}^{II}\} \quad (1)$$

$$\frac{d MMHg}{dt} = +k_{met}\{Hg^{II}\} - k_{demet} MMHg - k_{phdm}\{MMHg_{DOC} + MMHgCl\} - k_{met}\{MMHg\} + k_{phdm2} DMHg - \omega_s\{MMHg_{POC}\} + Ex_{200} \frac{MMHg_{200}}{C_{200}} + D_{200} \frac{MMHg_{200}}{C_{200}} - \frac{d MMHg_{phy}}{dt} \quad (2)$$

$$\frac{d Hg^0}{dt} = + (k_{phred} + k_{biored})\{Hg_{DOC}^{II} + HgCl_n\} - (k_{phox} + k_{biox})\{Hg^0\} + \alpha k_{phdm} + \{MMHg_{DOC} + MMHgCl\} - k_{vol}\left\{Hg_w^0 - \frac{Hg_{atm}^0}{K_H}\right\} \quad (3)$$

$$\frac{d DMHg}{dt} = + k_{met}\{MMHg\} - k_{phdm2}\{DMHg\} \quad (4)$$

Field observations suggest that particulate Hg dynamics are controlled by regenerative scavenging mechanisms dependent on adsorption, remineralization, and sinking, with little influence of desorption (Lamborg et al., 2016). In the coupled OGSTM-BFM-Hg model, the dynamics POC and DOC including sinking and

(Lamborg et al., 2016). In the coupled OGSTM-BFM-Hg model, the dynamics POC and DOC including sinking and degradation are spatially resolved by the BFM model, and their concentrations are read by the Hg model (Figs. 2 and 3) to calculate the partitioning of  $Hg^{II}$  and MMHg between particulate species (associated to organic detritus, i.e.,  $Hg^{II}_{POC}$  and  $MMHg_{POC}$ ) and dissolved species (associated to dissolved organic carbon, i.e.,  $Hg^{II}_{DOC}$  and  $MMHg_{DOC}$ , and ionic species, i.e.,  $HgCl_n$  and  $MMHgCl$ ). By combining POC and DOC concentrations with chemical partition constant  $K_D$  (Tab. S1) (Choe et al., 2003; Choe and Gill, 2003; Lamborg et al., 2016),

the fraction of each Hg species with respect to its total ( $f_{Hg-POC}$ ,  $f_{Hg-DOC}$ ,  $f_{HgCl}$ ,  $f_{MeHg-POC}$ ,  $f_{MeHg-DOC}$ ,  $f_{MeHgCl}$ ) is estimated (e.g., Eq. 5-7) fraction of each Hg species with respect to its total ( $f_{Hg-POC}$ ,  $f_{Hg-DOC}$ ,  $f_{HgCl}$ ,  $f_{MeHg-POC}$ ,  $f_{MeHg-DOC}$ ,  $f_{MeHgCl}$ ) is estimated (e.g., Eq. 5-7 for  $Hg^{II}$ ) assuming repartition at thermodynamic equilibrium. The fractions

are used to calculate concentrations of particulate and dissolved Hg species from the total pool of  $Hg^{II}$  and MMHg (e.g., Eq. 8). The pool of dissolved gaseous mercury species (DGM, i.e.,  $Hg^0$  and DMHg) is assumed to be entirely in the dissolved phase.

ha formattato: Apice

$$f_{Hg_{POC}} = \frac{Hg^{II}_{POC}}{Hg^{II}_{TOT}} = \frac{POC K_D Hg-POC}{1 + DOC K_D Hg-DOC + POC K_D Hg-POC} \quad (5)$$

$$f_{Hg_{DOC}} = \frac{Hg^{II}_{DOC}}{Hg^{II}_{TOT}} = \frac{DOC K_D Hg-DOC}{1 + DOC K_D Hg-DOC + POC K_D Hg-POC} \quad (6)$$

$$f_{HgCl} = \frac{HgCl_n}{Hg^{II}_{TOT}} = \frac{1}{1 + DOC K_D Hg-DOC + POC K_D Hg-POC} \quad (7)$$

$$Hg^{II}_{POC} = f_{Hg_{POC}} Hg^{II}_{TOT} \quad (8)$$

Once the partitioning is determined, the model computes the transformations fluxes based on first order rates ( $k_{3s}$ ,  $d^{-1}$  Tab. S2), the bioconcentration (Sect. 2.3) and bioaccumulation fluxes (Sect. 2.4), the sinking of  $Hg_{POC}$  and  $MMHg_{POC}$ , the advective transport within the model domain and at the model boundaries (i.e. Gibraltar Strait), and the exchange of  $Hg^0$  with the atmosphere. Microbial Hg methylation ( $k_{met} Hg^{II}$ ), reduction ( $k_{biores} \{Hg^{II}_{DOC} + HgCl_n\}$ ), and oxidation ( $k_{bioox} Hg^0$ ) are parameterized as functions of particulate organic matter remineralization (Zhang et al., 2020, 2014), which is read from the BFM model. The direct conversion of  $Hg^{II}$  to DMHg is assumed to be negligible, due to the low rates observed in the only dataset available for this process (Lehnher et al., 2011). Although several observations linked Hg methylation to oxygen consumption and organic matter remineralization in the water column, a full mechanistic understanding of

methylation and demethylation is still lacking (An et al., 2019; Wang et al., 2020). Here we assumed that both reactions involve the entire  $Hg^{II}$  and MMHg pools (Ortiz et al., 2015; Schaefer and Morel, 2009; Zhang et al., 2019). Photochemical transformations, i.e. photoreduction ( $k_{phred} \{Hg_{DOC}^{II} + HgCl_n\}$ ), photooxidation ( $k_{phox} Hg^0$ ), and photodegradation of MMHg ( $k_{phdem} \{MMHg_{DOC} + MMHgCl\}$ ) and DMHg ( $k_{phdm2} DMHg$ ) are assumed to act only on the dissolved fractions, and are a function of the attenuated shortwave flux (Zhang et al., 2014). MMHg photodegradation is assumed to yield both  $Hg^0$  and  $Hg^{II}$  ( $k_{phdm} \{MMHg_{DOC} + MeHgCl\}$ ) due to the contrasting results in experimental studies (Luo et al., 2020).

The gas-exchange flux of  $Hg^0$  with the atmosphere ( $k_{vol} \{Hg_w^0 - Hg_{atm}^0 / K_H\}$ ) is using the Nightingale's parameterization (Nightingale et al., 2000) for the rate constant  $k_{vol}$ , (Eq. (9)), which depends on wind speed ( $u_{10}$ ,  $m \cdot s^{-1}$ ) and on the ratio of Hg Schmidt number to  $CO_2$  Schmidt number ( $Sc_{Hg_w} / Sc_{CO_2_w}$ ).

$$k_{vol} = (0.222u_{10}^2 + 0.333u_{10}) \left( \frac{Sc_{Hg_w}}{Sc_{CO_2_w}} \right)^{-0.5} \quad (9)$$

Current knowledge on dynamics and concentrations of DMHg in the ocean and in the atmosphere does not allow a detailed modelling representation (Baya et al., 2015; Coale et al., 2018; De Simone et al., 2014; Melaku Canu et al., 2015; Nerentorp Mastromonaco et al., 2017; Rosati et al., 2018; Zhang et al., 2020), and simulated variations of DMHg (Eq. 4) depend on photodegradation, production upon MMHg methylation and advective transport. MMHg is uptaken from the water pool by phytoplankton ( $MMHg_{phy}$ ) (Sect. 2.3), and it is released from the biotic pool back to the water column by zooplankton excretion ( $Ex_{zoo} \frac{MMHg_{zoo}}{C_{zoo}}$ ) and death ( $D_{zoo} \frac{zooMMHg}{C_{zoo}}$ ) (Sect. 2.4). Loadings, initial and boundary conditions are presented in Sect. 2.6.

### 2.2.3 MMHg uptake by phytoplankton in the Hg model

The bioaccumulation model simulates the MMHg uptake by the phytoplankton PFTs of the BFM model assuming that the uptake flux (Eq. (10),  $nmol_{(Hg)} m^{-3}(w) d^{-1}$ ) decreases at high DOC concentrations and increases with phytoplankton Surface Area:Volume ratios ( $R_{SV\_PFT}$ ), following the empirical relation estimated by Schartup et al., (2018) from multi-species phytoplankton uptake data (Lee et al., 2017; Lee and Fisher, 2016). The bioaccumulation model also considers the phytoplankton density ( $\rho = 10^{-12} g_{(w.w.)} \mu m^{-3}(w.w.)$ ), wet weight biomass ( $B_{w.w.,PFT}$ , in  $g_{(w.w.)} m^{-3}(w)$ ), and the water MMHg concentrations ( $\{MMHg\}_w$ , pM). Parameters values are given in Tab. S3.

$$\frac{d MMHg_{phy, PFT}}{dt} = 0.118 \cdot R_{SV\_PFT} \cdot \exp^{(-0.08 \cdot DOC)} \frac{1}{\rho} B_{w.w., PFT} \frac{\{MMHg\}_w}{10^3} \quad (10)$$

205  $B_{w,w,PFT}$  were derived from the plankton biomasses expressed on a intracellular carbon content basis ( $C_{PFT}$ , in  $\text{mg}_{(C)}\text{m}^{-3}_{(w)}$ ), by adopting a carbon to Wet Weight conversion factors (Tab. S4) that we estimated from a dataset of experimental data for various phytoplankton and zooplankton species (Jørgensen et al., 1979; Mahlmann et al., 2008).

#### 2.2.4 Zooplankton bioaccumulation in the Hg model

According to previous studies (Schartup et al., 2018; Zhang et al., 2020), MMHg bioaccumulation in zooplankton is mostly driven by grazing (>80%), therefore the trophic transfer of MMHg from phytoplankton to zooplankton PFTs (heterotrophic nanoflagellates, microzooplankton, omnivorous mesozooplankton, and carnivorous mesozooplankton) in the model is set proportionally to the carbon (C) transfer, neglecting direct uptake from seawater. Thus, the bioaccumulation of MMHg in each zooplankton PFT (Eq. (11)) depends on carbon grazing fluxes ( $G_{200,PFT}$ ,  $\text{mg}_{(C)}\text{m}^{-3}\text{d}^{-1}$ ) and the MMHg:C ratio of the preys that are grazed ( $\frac{MMHg_{phy,PFT}}{C_{phy,PFT}}$ ,  $\text{nmol}_{(Hg)}\text{mg}^{-1}_{(C)}$ ). MMHg release to the water pool occurs following carbon excretion ( $EX_{200,PFT}$ ) and zooplankton death ( $D_{200,PFT}$ ,  $\text{mg}_{(C)}\text{m}^{-3}$ ), and depends on the variable MMHg:C quota ( $\frac{MMHg_{200,PFT}}{C_{200,PFT}}$ ,  $\text{nmol}_{(Hg)}\text{mg}^{-1}_{(C)}$ ) in each zooplankton group.

$$\frac{d MMHg_{200,PFT}}{dt} = G_{200,PFT} \frac{MMHg_{phy,PFT}}{C_{phy,PFT}} - EX_{200,PFT} \frac{MMHg_{200,PFT}}{C_{200,PFT}} - D_{200,PFT} \frac{MMHg_{200,PFT}}{C_{200,PFT}} \quad (11)$$

#### 2.2.5 Indicators for MMHg bioaccumulation and biomagnification

220 To compare the model content of MMHg in phytoplankton and zooplankton against experimental data, the output in  $\text{nmol}_{(Hg)}\text{m}^{-3}_{(w)}$  was converted into  $\text{ng}_{\text{g}_{w,w}^{-1}}$  by computing the quota of MMHg ( $Q_{MMHg,PFT}$ , Eq. (12)) to plankton wet weight ( $B_{w,w,PFT}$ ,  $\text{g}_{w,w}\text{m}^{-3}_{(w)}$ ) and correcting for the molar mass of Hg ( $200.59\text{ g mol}^{-1}$ ).

$$Q_{MMHg,PFT} = \frac{MMHg_{phy,PFT}}{B_{w,w,PFT}} 200.59 \quad (12)$$

The bioconcentration factor (BCF,  $1\text{ kg}^{-1}$ ) is used to synthesize the enrichment of Hg in plankton with respect to water concentrations (Harding et al., 2018; McGeer et al., 2003), and due to the normalization for MMHg water levels, it allows better intercomparability across ecosystems than Hg concentrations. We calculated BCFs (Eq. (13)) for each plankton PFT as the ratio between the quota  $Q_{MMHg,PFT}$  and water MMHg concentrations, using model output at monthly resolution spatially averaged. The logarithmic scale is often used to handle BCF values (e.g. McGeer et al., 2003).

$$\text{BCF} = 10^6 \frac{Q_{MMHg,PFT}}{MMHg^w 200.59} \quad (13)$$

ha formattato: Apice

ha formattato: Apice



The trophic magnification factor (TMF) is used to explore biomagnification across ecosystems, by expressing the increase of Hg along [with](#) trophic levels (Alava et al., 2018; Harding et al., 2018). TMF is usually calculated in field studies of the whole-food web assessing both concentrations of pollutants and trophic levels [through](#) nitrogen isotopes. Here, in agreement with other modelling studies (Wu et al., 2021, 2020; Zhang et al., 2020), TMFs were estimated from the ratio of the MMHg quota in zooplankton PFTs to that of grazed phytoplankton PFTs (Eq. (14)). The analysis was carried out considering the model plankton food web as composed [of](#) a lower trophic level “herbivorous” part and an upper “omnivorous” part.

$$235 \quad \text{TMF} = \frac{Q_{\text{MMHg, zoo-PFTs}}}{Q_{\text{MMHg, phy-PFTs}}} \quad (14)$$

### 2.2.6 Initial conditions, boundary conditions and forcings

[Model](#) initial conditions, boundary conditions, and physical forcings [at](#) monthly resolution are set [according to](#) Lazzari et al., (2021). Initial conditions for Hg species ([Tab. S5](#)) in Mediterranean subbasins (Fig. 1) are extrapolated from published data from different investigations in the Mediterranean Sea (Cossa et al., 2017; Cossa and Coquery, 2005; Ferrara et al., 2003; Horvat et al., 2003; Kotnik et al., 2015, 2007) and boundary conditions are set in agreement with the observations from the GEOTRACES GA03 meridional transect (Bowman et al., 2015). [River Hg load is estimated based on dissolved Hg concentration, assuming 3 pM and 3.5% of MMHg \(Cossa et al., 2017\), using a higher concentration for three rivers that are known to be highly impacted by mining \(Isonzo-Soča river, 25 pM\) \(Hines et al., 2000\), industrial activities \(Po river, 6 pM\) \(Vignati et al., 2008\) or both of them \(Tiber river, 6 pM\) \(Lanzillotta et al., 2002; Rimondi et al., 2019\), assuming MMHg is the 1% \(Hines et al., 2000\). Further, a sensitivity simulation accounting for the load of particulate Hg was carried out \(Sect. 2.3.3\) to investigate model uncertainty sensitivity simulation accounting for the load of particulate Hg was carried out \(Sect. 2.3.3\) to investigate model uncertainty regarding this source.](#) The atmospheric  $\text{Hg}^0$  concentration is set to a constant value  $Hg_{\text{atm}}^0 = 1.6 \text{ ng m}^{-3}$  (Andersson et al., 2007; Fantozzi et al., 2013; Gärdfeldt et al., 2003), and the atmospheric deposition of  $\text{Hg}_T$  is set to  $67.5 \text{ Mg y}^{-1}$ , the 2% of which is MMHg (Cossa et al., 2022, 2017). The Hg concentrations in the Black Sea outflow at the Dardanelles strait are set at 0.2 pM in agreement with the observations from the GEOTRACES GA04 cruise and modelled fluxes (Rosati et al., 2018).

### 2.3 Model sensitivity to key parameters and processes

255 [A set of sensitivity simulations was implemented to investigate model uncertainty and improve the fit against experimental observations, initially showing substantial underestimation of MeHg concentrations maxima. The sensitivity simulations aimed at assessing the impacts of variations of the values of the sinking velocity of organic detritus and associated Hg species \(Sect. 2.3.1\), and of the coefficient for Hg methylation rates \(Sect. 2.3.2\), as well as the loading of Hg from rivers \(Sect. 2.3.3\).](#)

260 [which is a process poorly characterized by field observations \(Liu et al., 2021\). All the analyses of model results focus on the same simulation, which adopts a sinking velocity of 10 m d<sup>-1</sup>, a methylation rate constant higher than the one used in global modeling \(Zhang et al., 2020\), and accounts only for dissolved input of Hg from rivers,](#)

ha formattato: Apice

ha formattato: Inglese (Stati Uniti)

### 2.3.1 Sensitivity [simulations for POC sinking velocity](#)

265 A sensitivity analysis of POC sinking velocity was carried out, hypothesizing that a change in this parameter would impact the vertical distribution of all Hg species due to a change in the distribution and remineralization of POC, and in the transport of particulate Hg and MeHg. We also speculate that a deeper occurrence of POC remineralization leading to deeper MeHg maximum, could result in a decreased amount of MeHg photochemically degraded and thus in higher MeHg concentrations. [The current version of BFM model includes only one class of non-living organic detritus \(POC\) that is a sink for all the plankton state variables \(Vichi et al., 2015\), resulting in a homogenous POC sinking velocity representative of an ecosystem-averaged dynamic.](#) In the field, organic particles and aggregates that originate from a continuous size-spectrum of planktonic cells of various composition, show a wide range of sinking speeds (Cael et al., 2021).

The [reference](#) model simulation was run by adopting the default POC sinking velocity of 3 m d<sup>-1</sup> [previously](#) used to model The

270 [reference](#) model simulation was run by adopting the default POC sinking velocity of 3 m d<sup>-1</sup> [previously](#) used

275 to model the biogeochemistry of the Mediterranean Sea ([Lazzari et al., 2021, 2012](#)).

[Here](#), two additional sensitivity simulations were run, by setting the POC sinking velocity at 10 and 20 m d<sup>-1</sup>, assuming community-averaged cell diameters of 35 and 50 μm, respectively.

ha formattato: Apice

### 2.3.2 Sensitivity [simulations for Hg methylation](#)

280 Hg methylation [was](#) parameterized in the model by scaling the flux of POC remineralization for a constant  $x_{met}$  (Tab. S2), adopting the same value used in a global ocean model (Zhang et al., 2020), due to [the](#) unavailability of more specific data. We explored the sensitivity of modelled MeHg concentrations to a threefold increase of  $x_{met}$ , as well as to an alternative parameterization that included both POC and DOC remineralization flux (Eq. S10).

### 2.3.3 Sensitivity [simulation for river Hg load](#)

285 [The largest Mediterranean rivers are characterized by proximal-accumulation-dominated dispersal system, i.e., deltaic systems with fast and substantial \(>50-90%\) sediment accumulation in the proximity of their mouth \(Walsh and Nittrouer, 2003\). Consistently with this picture, a recent budget for the Mediterranean Sea estimated that the magnitude of total Hg input from rivers \(6 Mg y<sup>-1</sup>\) is comparable to the Hg flux to the shelf sediments \(6.8 Mg y<sup>-1</sup>\), suggesting that most of the Hg associated with riverine particles settle before reaching the open ocean \(Cossa et al., 2022\). We, therefore, included only the dissolved load of Hg and MMHg in the reference simulation](#)

290 [and explored the uncertainty related to this choice with a sensitivity simulation accounting for the total load Hg species, i.e., including both the particulate and dissolved inputs of Hg<sup>II</sup> and MMHg. Limited data are available to characterize the spatial and temporal variability of these sources. The most robust observations are from a time-series \(2008-2010\) for the Rhône River \(Cossa et al., 2017\) indicating  \$0.85 \pm 0.45\$  nmol g<sup>-1</sup> of Hg<sub>T</sub> and  \$0.017 \pm 0.008\$  nmol g<sup>-1</sup> of MMHg. Assessments in the Ebro River, impacted by an industrially polluted water reservoir, and in the Po River, which drain the largest Italian industrial and agricultural areas, found respectively 4.9 nmol g<sup>-1</sup> and 1.15 nmol g<sup>-1</sup> of particulate Hg<sub>T</sub> at the river mouth, also highlighting the role of episodic stormy event in transporting large amounts of particles and associated pollutants \(Palanques et al., 2020, Vignati et al., 2003\). Further, at the mouth of the Soča/Isonzo River, impacted by upstream Hg mining, concentrations of unfiltered Hg higher than 200 pM have been reported \(Hines et al., 2000\). Hg loads for the Mediterranean tributary were estimated based on this information as synthesized in Tab. S6, also qualitatively referring to the spatial distribution of Hg stock and erosion fluxes in European topsoils \(Panagos et al., 2021\) and other information on anthropogenic activities \(Ahmed et al., 2018\). In the reference simulation, including only the dissolved input, the loading estimate is 0.28 Mg y<sup>-1</sup> for total dissolved Hg \(and 0.008 Mg y<sup>-1</sup> for dissolved MMHg\), while in the simulation with total Hg inputs the loading is about 4.6 Mg y<sup>-1</sup> including 0.27 Mg y<sup>-1</sup> of MMHg. Despite the relatively high mean concentrations \(Tab. S6\) assumed, the estimated Hg<sub>T</sub> load is slightly lower than the estimate \(6 Mg y<sup>-1</sup>\) from Cossa et al., \(2022\), most likely because the water discharge used in that work \(>350 km<sup>3</sup> y<sup>-1</sup>\) is higher than the total discharge used in this model setup \(>291 km<sup>3</sup> y<sup>-1</sup>\). On the other hand, the load to the Mediterranean Sea from solely European rivers \(2.9 Mg y<sup>-1</sup>\) estimated from Hg concentrations in topsoils and water erosion rates from river catchments \(Panagos et al., 2021\) is slightly lower than the load from European rivers in our model setup \(3.25 Mg y<sup>-1</sup>\). Finally, all these estimates are lower than the 18 Mg y<sup>-1</sup> computed by \(Liu et al., 2021\) for the Mediterranean Sea through a global river model explicitly considering water discharge, suspended solids, and Hg loadings. Based on these calculations, Liu et al., \(2021\) proposed a global river load \(1000 Mg y<sup>-1</sup>\) much higher than the estimate from the latest global mercury assessment \(300 Mg y<sup>-1</sup>\) \(UNEP, 2018\). They also estimated that the 70% of the load is buried in coastal and shelf sediment.](#)

### 3 Results and discussion

#### 3.1 Model sensitivity and uncertainty

315 The sensitivity analysis showed that the sinking [rate of organic detritus \(POC\)](#) is an important control on the vertical distribution of MeHg (i.e., the shape of the vertical profile) [along the water column](#) but has little effect on the values of [MeHg concentrations maxima and the distribution of inorganic Hg species](#) (Supplemental Sect. S1.1 and Figs. S1 and S2). [On the other hand, the increase of sinking velocity from 3 to 10 m d<sup>-1</sup> improved the agreement of modelled seasonal fluxes of POC at 200 m depth with available observations \(Ramondenc et al., 2016\) \(Supplemental Sect. S1.1 and Fig. S3\).](#) The sensitivity [analysis](#) also showed that [an increase in the coefficient for Hg methylation \( \$x\_{mer}\$ \) results in a higher agreement with observed MeHg concentrations \(Cossa et al., 2022,](#)

ha formattato: Apice

2009), while the inclusion of DOC remineralization flux results in an overestimation of surficial MeHg concentrations (Supplemental Sect. S1.2 and Fig. S3).

325 The inclusion of higher riverine  $Hg^{II}$ , MMHg, and POC inputs does not improve the agreement between modelled and observed concentrations of MeHg (Supplemental Sect. S1.3 and Figs. S5-S10), suggesting that the underestimation of MeHg maxima in subsurface waters is not due to an underestimation of watershed sources. These results also corroborate the idea that a substantial fraction of particulate Hg and MeHg carried by rivers settles in coastal areas along with POC (Fig. S5), as estimated in a recent budget based on field observations (Cossa et al., 2022). Nonetheless, large uncertainties in the spatial and temporal variability of riverine loadings and coastal processes remain to be addressed both at the basin and  
330 global scale (Cossarini et al., 2021; Liu et al., 2021).

The underestimation of MeHg in the model does not appear to be related to inorganic Hg availability, since the concentrations of  $Hg_T$  are within the experimental uncertainty of the data (Fig. S11).

335 Modelled fluxes of  $Hg_T$  and  $Hg^0$  compare well with other budget estimates (Cossa et al., 2022; Žagar et al., 2007).

The net exchange of gaseous  $Hg^0$  with the atmosphere indicates  $44.8 \text{ Mg y}^{-1}$ , which is close to a previous estimate ( $50 \text{ Mg y}^{-1}$ ). The net exchange of gaseous  $Hg^0$  with the atmosphere indicates  $44.8 \text{ Mg y}^{-1}$ , which is close to a previous estimate ( $50 \text{ Mg y}^{-1}$ ) based on aquatic biogeochemical modelling (Žagar et al., 2007) and slightly lower than the flux adopted in the budget from Cossa and coauthors ( $67.5 \text{ Mg y}^{-1}$ ). Considering both  $Hg^0$  exchange and atmospheric  
340 deposition of  $Hg^{II}$  (Sect. 2.2.6 and Fig. 3), the net exchange of Hg species ( $\sim 7 \text{ Mg y}^{-1}$ ) is here significantly lower than the estimate ( $29.8 \text{ Mg y}^{-1}$ ) from Cossa et al., (2020). However, while the latter estimate is based on an atmospheric model assuming a constant ocean surface  $Hg^0$  concentrations (Gencarelli et al., 2014), here, the flux is estimated accounting for 3D dynamics in the marine system, including sequestration of Hg species from surface waters due to the biological carbon pump. Recent evidence from isotopes studies pointed out that the ocean might be a net sink for atmospheric Hg, rather than a net source  
345 (Jiskra et al., 2021).

The modelled export of  $Hg_T$  from the Alboran Sea to the Atlantic Ocean is  $9.3 \text{ Mg y}^{-1}$ , close to the value ( $9.7 \text{ Mg y}^{-1}$ ) estimated by Cossa et al., (2022). On the other hand, our estimate ( $2.5 \text{ Mg y}^{-1}$ ) of MeHg outflow is significantly lower than the  $5.6 \text{ Mg y}^{-1}$  of the budget by Cossa et al., (2022), even assuming an increased value for  $x_{met}$  and, consequently, of subsurface MeHg.

350 All in all, a calibration of the parameter  $x_{met}$  appears appropriate based on the current understanding, also considering that the initial guess for this parameter come from a global ocean application (Zhang et al., 2020). Indeed, such a global model study underestimated the observed MeHg concentrations in the Mediterranean Sea, while reproducing with good agreement, or overestimating, observations from various cruises in the North Atlantic and Pacific Ocean, pointing out the need to better  
355 resolve spatial and temporal variability of biological processes and linked Hg dynamics (Zhang et al., 2020). A comprehensive

ha formattato: Apice

ha formattato: Apice

validation of the OGSTM-BFM biogeochemical variables (Cossarini et al., 2021) highlighted good model accuracy in surface water but higher mismatches with observed oxygen and nutrients concentrations in the mesopelagic zone, attributed to uncertainties in remineralization and deep ventilation processes, which also affect methylation dynamics. In spite of uncertainties remaining to be addressed, the OGSTM-BFM-Hg model is able to reproduce the spatial gradients observed in the Mediterranean Sea, testifying the improvements in capability to simulate Hg dynamics (Žagar et al., 2014, 2007) through the coupling with key biological processes, e.g. the carbon pump and microbial loop (Bowman et al., 2020; Cossa et al., 2017, 2009; Heimbürger et al., 2010; Monperrus et al., 2007; Munson et al., 2018; Sunderland et al., 2009).

### 3.2 MeHg distribution in the water of Mediterranean Sea

The zonal and vertical gradients of MeHg concentrations reproduced by the OGSTM-BFM-Hg model show the highest concentrations in subsurface waters of the most productive subbasins of the Mediterranean Sea (Fig. 4), consistently with the available observations (Cossa et al., 2009). Modelled vertical profiles of MeHg concentrations (Fig. 5) are in good agreement with the observations in the Southern Adriatic Sea (*Sad*, Fig. 5a), and are in the lower range of the observations for the North Western Mediterranean (*Nwm*, Fig. 5b) and Ionian (*Ion*, Fig. 5c) subbasins.

In the *Sad* subbasin, a progressive buildup of MeHg subsurface maxima (up to 0.18 pM) is predicted from April to September, driven by an increase in primary production triggering higher POC remineralization and in turn higher Hg methylation rate constants  $k_{met}$  (Fig. S4). However, while  $k_{met}$  are maxima in April, and net methylation fluxes (Fig. 6) are maxima in June ( $0.45 \text{ pmol m}^{-3} \text{ d}^{-1}$ ), MeHg concentrations are maxima in September and remain stable until October (Fig. 5), highlighting the importance of water stratification for the formation of the subsurface maxima. Figure 6 also shows that net demethylation prevails throughout the year in deep waters (except for weak positive methylation in *Sad* and *Tyr* during summer), and for most of the year in surface waters, suggesting that the presence of MeHg in surface and deep water depends on its formation in the intermediate waters and diapycnal mixing.

Modelled vertical profiles of MeHg in the oligotrophic *Ion* subbasin (Fig. 5c) have lower maxima (up to 0.16 pM) and a smoother concentration gradient compared to the more productive waters of the *Nwm* (up to 0.24 pM). The West-East gradient is sustained by the highest methylation rates (Fig. S12) in the Western Mediterranean, driven by higher primary productivity and remineralization of organic detritus, and it is further reinforced by high rates of both photochemical and biological MeHg degradation in the Eastern subbasins (Fig. S12), due to the highest water temperature, irradiance, and deeper penetration of shortwave radiation due to the low plankton biomass.

### 3.4 Modelled MMHg in phytoplankton and zooplankton

The spatial and temporal distributions of modelled MMHg in phytoplankton ( $MMHg_{phy}$ ) and zooplankton ( $MMHg_{zoo}$ ) of the Mediterranean Sea (Fig. 7) are overall comparable to the concentrations of particulate MMHg ( $0.7 \pm 1.3 \text{ pmol m}^{-3}$ ) measured in the Atlantic Ocean (Bowman et al., 2015). The model reproduced a seasonal increase in  $MMHg_{phy}$  (Fig. 7a) during late spring and summer that is driven by blooms of picophytoplankton (Fig. S13) combined with an increase in MMHg

ha formattato: Tipo di carattere: Corsivo

ha formattato: Tipo di carattere: Corsivo

ha formattato: Tipo di carattere: Corsivo

ha formattato: Tipo di carattere: Corsivo

ha formattato: Pedice

ha formattato: Tipo di carattere: Corsivo

ha formattato: Tipo di carattere: Corsivo

ha formattato: Tipo di carattere: Corsivo

availability in surface water (Fig. S14). The amount of MMHg bioaccumulated by picophytoplankton ( $MMHg_{phy,P3}$ , Fig. S15) is high (up to  $0.6 \text{ pmol}_{(Hg)} \text{ m}_{(w)}^{-3}$ ) compared to the bioaccumulation by other phytoplankton PFTs (up to  $0.02 \text{ pmol}_{(Hg)} \text{ m}_{(w)}^{-3}$ , Fig. S16-S18) due to the model assumption of increasing bioconcentration capacity with decreasing phytoplankton cell size (Sect. 2.3). However, not all the picophytoplankton blooms result in high values of  $MMHg_{phy}$ : the strongest blooms of picophytoplankton, occurring in March and April at 25 m depth (Fig. S13), have a marginal impact on bioaccumulation, especially in the easternmost subbasins, due to the very low concentrations of MMHg in the most surficial waters (Fig. S14). On the other hand, much weaker blooms of picophytoplankton occurring from May to August slightly deeper in the water column (35 and 45 m depth) lead to a maximum in phytoplankton MMHg concentrations (Fig. 7a) because of higher water MMHg concentrations at these depths during these months (Fig. S14). The average  $MMHg_{phy,P3}$  is lower in the *Alb* subbasin than in the *Sad* subbasin (Tab. 1), the latter being characterized by higher availability of MMHg at 35-45 m depth and higher biomasses of picophytoplankton during summer (Fig. S13 and S14). The hypothesis of the cell size-effect on bioconcentration is the best synthesis of available knowledge (Schartup et al., 2018), however, the experimental study from which this relationship was derived, also showed deviations from this pattern and temperature induced effects, possibly due to phagocytosis of Hg-OM compounds by mixotroph organisms such as dinoflagellates (Lee and Fisher, 2016). One of the few field studies assessing the size-effect on Hg bioaccumulation in plankton (Gosnell and Mason, 2015) found an increase in MeHg% but not in MeHg content for smaller plankton size ( $< 5 \mu\text{m}$ ), however, the size classes analysed by that study do not overlap well with the functional groups of OGSTM-BFM-Hg model. More field, in vitro, and modelling studies are needed to disentangle the dynamics underlying key processes for Hg bioaccumulation.

The highest concentrations of  $MMHg_{zoo}$  (Fig. 7b) are predicted from June to September at 35 m-depth, showing a delay of about one month with respect to the temporal evolution of  $MMHg_{phy}$  due to the combined impacts of plankton phenology and trophic interactions. Heterotrophic nanoflagellates bioaccumulate much more MMHg (up to  $0.5 \text{ pmol m}^{-3}$ , Fig. S19) than other zooplankton PFTs (up to  $0.1 \text{ pmol m}^{-3}$ , Fig. S20-S22) because they feed on picophytoplankton (Fig. 8) which is more enriched in MeHg than other PFTs and is an important driver for the distribution of  $MMHg_{zoo}$ . However, in spite of heterotrophic nanoflagellates being always abundant from March to October (Fig. S23), and most abundant in the eastern subbasins, the highest MMHg bioaccumulation occurs when the increase of the nanoflagellates population is coincident with an enrichment of MMHg in phytoplankton (*i.e.*, in western subbasins, as well as in the Adriatic and part of the Ionian Sea during summer).

The mean MMHg quota ( $Q_{MMHg,PFT}$ ) in phytoplankton of the Mediterranean Sea is about  $3.0 \text{ ng g}_{w,w}^{-1}$  for picophytoplankton,  $0.3 \text{ ng g}_{w,w}^{-1}$  for autotrophic nanoflagellates,  $0.03 \text{ ng g}_{w,w}^{-1}$  for diatoms, and  $0.04 \text{ ng g}_{w,w}^{-1}$  for large phytoplankton. The spatial variability is highlighted by comparing the quotas estimated for the *Alb* and *Sad* subbasins (Tab. 1) that are in the lower and upper range of the values for the Mediterranean Sea. Modelled values are comparable with the few observations available for open waters of the central Pacific Ocean ( $0.1\text{-}4 \text{ ng g}_{w,w}^{-1}$ ) (Gosnell & Mason, 2015), and of the Northwest Atlantic Ocean ( $0.15 \pm 0.06 \text{ ng g}_{w,w}^{-1}$ ) (Hammerschmidt et al., 2013), as well as with data from various coastal and shelf ecosystems (Harding et al., 2018). The speciation of Hg in phytoplankton groups of the Mediterranean Sea has never been assessed

ha formattato: Apice

ha formattato: Tipo di carattere: Corsivo

ha formattato: Tipo di carattere: Corsivo

ha formattato: Tipo di carattere: Corsivo

(Cinnirella et al., 2019). The MMHg quota was about  $0.14 \pm 0.1 \text{ ng g}_{w.w}^{-1}$  in seston of diameter 80–200  $\mu\text{m}$  sampled in the Gulf of Lions during spring and autumn 2004–2006 (Cossa et al., 2012).

The mean  $Q_{MMHg,PFT}$  in zooplankton are  $0.8 \text{ ng g}_{w.w}^{-1}$  for heterotrophic nanoflagellates,  $0.3 \text{ ng g}_{w.w}^{-1}$  for microzooplankton,  $0.6 \text{ ng g}_{w.w}^{-1}$  for omnivorous mesozooplankton, and  $0.9 \text{ ng g}_{w.w}^{-1}$  for carnivorous mesozooplankton. The MMHg quota in carnivorous zooplankton ( $Q_{MMHg,Z3}$ ) estimated for the *Sad* subbasin is much higher ( $3.60 \pm 2.2$ ) than the average value due to the high MMHg accumulation in the whole food web (Tab. 1). However, since biomasses of carnivorous zooplankton in the *Sad* are very low (Fig. S16), the overall content of MMHg in this group ( $MMHg_{zoo,Z3}$ ) is lower ( $1.0 \cdot 10^{-3} \pm 2.7 \cdot 10^{-4}$ ) than in the *Alb* subbasin ( $1.9 \cdot 10^{-2} \pm 1.6 \cdot 10^{-3}$ ).

The modelled zooplankton quotas compare well with the observations of MMHg in mesozooplankton of the Gulf of Lions, which was  $0.52 \pm 0.39 \text{ ng g}_{w.w}^{-1}$  for the size range 200–500  $\mu\text{m}$ ,  $0.57 \pm 0.39 \text{ ng g}_{w.w}^{-1}$  for the size range 500–1000  $\mu\text{m}$ , and  $1.8 \pm 1.3 \text{ ng g}_{w.w}^{-1}$  for zooplankton  $>200 \mu\text{m}$  (Cossa, 2012). MMHg measured in the '90s in zooplankton in the Gulf of Trieste (*Nad*, Fig. 3) *Hg hotspot* was  $2.1 \pm 2.3 \text{ ng g}_{w.w}^{-1}$  (Horvat et al., 2014, 1999), consistently with the fact that the Gulf of Trieste is an upper bound for the Mediterranean, being subjected to high loadings of legacy Hg from the *Soča*-Isonzo river (Hines et al., 2000) and coastal lagoons (Melaku Canu et al., 2015, *Rosati et al., 2020*).

### 3.3 Bioconcentration Factors and Trophic Magnification Factors

Modelled BCFs for phytoplankton PFTs of the Mediterranean Sea range 3.7–6.5, which is slightly lower than the range (4.3–6.8) reported for phytoplankton from the central Pacific (Gosnell and Mason, 2015) and is higher than the ranges for Long Island Sound (2.6–5.5) (Gosnell et al., 2017) and other coastal and shelf sites of the world (3.1–4.4) (Harding et al., 2018).

Higher BCFs in open waters than in coastal areas are consistent with the enhanced Hg bioavailability in the open sea inferred by other authors (Gosnell and Mason, 2015; Schartup et al., 2015), which in the model is approximated through the inverse relationship between MMHg uptake and DOC (Eq. (10)). Modelled zooplankton BCFs in the Mediterranean Sea span from 4.0 to 6.4, comparable to the BCFs estimated for mesozooplankton (4.0–6.5) in the Pacific Ocean (Gosnell and Mason, 2015). The trophic interactions among PFTs simulated by the model can be subdivided into a lower “herbivorous” part of the food web and an upper “omnivorous” part of the food web (Fig. 8). In the lower part of the food web, heterotrophic nanoflagellates (2–20  $\mu\text{m}$ ) graze on bacteria ( $<1 \mu\text{m}$ ) and picophytoplankton (0.2–2  $\mu\text{m}$ ), while microzooplankton (20 – 200  $\mu\text{m}$ ) grazes on heterotrophic and autotrophic nanoflagellates (2–20  $\mu\text{m}$ ), diatoms (200– 20  $\mu\text{m}$ ), and occasionally on other PFTs. In the upper part of the food web, the omnivorous mesozooplankton (200–2000  $\mu\text{m}$ ) preys on microzooplankton and all the phytoplankton PFTs  $>2 \mu\text{m}$ , while carnivorous mesozooplankton (200–2000  $\mu\text{m}$ ) preys on omnivorous mesozooplankton and large phytoplankton ( $>100 \mu\text{m}$ ). The highest BCFs (and  $Q_{MMHg,PFT}$ ) are predicted for picophytoplankton and carnivorous zooplankton (Tab. 1 and Fig. 8). Heterotrophic nanoflagellates display lower bioaccumulation than picophytoplankton because they also feed on bacteria and autotrophic nanoflagellates that ‘dilute’ the MMHg intake (Fig. 8). Microzooplankton and omnivorous zooplankton, which have an intermediate position in the food web, have bioaccumulation levels comparable to those of heterotrophic nanoflagellates. The effect of biomagnification is visible only in carnivorous zooplankton, having much

ha formattato: Tipo di carattere: Corsivo

ha formattato: Tipo di carattere: Corsivo

ha formattato: Tipo di carattere: Corsivo

455 higher BCFs than their prey (Tab. 1). These dynamics are consistent with a global model taking into account a more complex plankton food web (366 PFTs) that found highest MMHg levels in phytoplankton than in their predators, and biomagnification in the highest trophic levels with high food intake (Wu et al., 2021).

Trophic magnification factors (TMFs) were calculated for each subbasin of the [Mediterranean](#) Sea for the lower and upper parts of the food web. Low TMFs (range 0.05-0.38) were estimated for the lower food web indicating [the](#) absence of biomagnification (Fig. 9a), and higher TMFs (range 0.15-2.60) were estimated for the upper food web (Fig. 9b), in agreement with previous modelling studies suggesting that MMHg biomagnification between small zooplankton groups and phytoplankton is unlikely to happen (Wu et al., 2021, 2020; Zhang et al., 2020). Biomagnification (TMF>1) in the upper food web (Fig. 9b) occurs only in subbasins with relatively abundant biomasses of carnivorous zooplankton (Fig. S24), namely in the [Alb](#) and [Swm](#) subbasins. The TMF for the [Alb](#) subbasin ( $2.4 \pm 0.28$ ) is lower than but comparable to the biomagnification from microseston to zooplankton (TMF=4) estimated from field data for the Northwest Atlantic Ocean (Hammerschmidt et al., 2013). The other Mediterranean subbasins, due to the absence or very low abundance of carnivorous mesozooplankton ( $<0.05 \text{ mg}_{(C)} \text{ m}^{-3}$ ), have a shorter food web and lower TMFs ( $<1$ ). Although oligotrophy tends to favour longer food webs enhancing biomagnification, in extremely oligotrophic ecosystems the very low primary production can limit the presence of carnivorous zooplankton populations, lowering the bioaccumulation potential (Wu et al., 2021). The TMFs $<1$  for the upper part of the food web are comparable to the estimates made with a global model for the most oligotrophic ocean regions such as the South Pacific [Cyre](#), the North Atlantic gyre, and the South Atlantic gyre (Wu et al., 2021).

#### 4 Conclusions

We developed [and released](#) the OGSTM-BFM-Hg model, a numerical state of the art model tracking the biogeochemistry of the main marine Hg species ( $\text{Hg}^{\text{II}}$ ,  $\text{Hg}^0$ , MMHg, and DMHg) [fully](#) coupled to the biogeochemistry of plankton and nutrients. The model, applied to a [high-resolution](#) 3D domain of the Mediterranean Sea, successfully captured the zonal and vertical variability of MeHg concentrations reproducing a decreasing MeHg gradient from West to East that is supported by the available observations. Sensitivity analysis showed that the agreement with observed MeHg concentrations and POC fluxes was improved by adopting an intermediate sinking speed for organic detritus. [Modelled MeHg concentrations also improved](#) by increasing the [coefficient](#) constant for Hg methylation [rate](#), while the inclusion of the of dissolved [organic carbon remineralization in the equation for Hg methylation](#) increases the mismatch between model and observations, suggesting that this process might not be important in shaping MeHg distributions.

[Sensitivity simulations on river Hg loadings corroborate the idea that in the Mediterranean Sea most of the inputs of particulate Hg \(and POC\) from rivers tend to sink in coastal and shelf areas and have a limited impact on open sea dynamics. However, as pointed out in a recent reassessment of global river inputs \(Liu et al., 2021\) there is a need to better assess the spatial and](#)

ha formattato: Tipo di carattere: Corsivo

ha formattato: Tipo di carattere: Corsivo

ha formattato: Tipo di carattere: Corsivo



[temporal variability of riverine loadings, especially in relation to extreme events and their increasing occurrence driven by climate changes.](#)

Model results highlight that summer stratification of the water column is an important process for the buildup of a sub-surficial maximum of MeHg concentrations, while the occurrence of deep convection in winter results in substantial redistribution of MeHg smoothing the vertical profiles. A decrease in winter convection events linked to increasing water temperature, which has already been observed in recent years in the Mediterranean Sea, seems to limit MeHg redistribution in the water column causing higher water MeHg concentrations in the biologically active zone and, in turn, higher plankton exposure. In fact, spatial and temporal variability of plankton bioaccumulation in the model is controlled by plankton phenology and by the availability of MMHg at the depths at which plankton blooms occur. The biomagnification potential is stronger in productive areas of the Mediterranean Sea characterized by high biodiversity and longer food web length with a significant presence of carnivorous zooplankton, such as the *Alb* and *Swm* subbasins.

#### Acknowledgments

The research has been partially funded by the PRIN project ICCO (Impacts of climate change on the biogeochemistry of contaminants in the Mediterranean Sea) [and the interreg MED project SHAREMED.](#)

#### 500 Code availability

The OGSTM-BFM-Hg model code is publicly available at Zenodo repository with DOI <https://doi.org/10.5281/zenodo.5851442> (Rosati et al., 2022).

#### References

- 505 [Ahmed, A. M. A., Purwanto, P., and Sunoko, H. R.: Consequences of Mercury Used by Artisanal and Small-Scale Gold Mining Processes a Case of River Nile State Sudan, J. Ecol. Eng., 20, 106–115, 2019.](#)
- Alava, J. J., Cisneros-Montemayor, A. M., Sumaila, U. R. and Cheung, W. W. L.: Projected amplification of food web bioaccumulation of MeHg and PCBs under climate change in the Northeastern Pacific, Sci. Rep., 8(1), 1–12, doi:10.1038/s41598-018-31824-5, 2018.
- Amos, H. M., Sonke, J. E., Obrist, D., Robins, N., Hagan, N., Horowitz, H. M., Mason, R. P., Witt, M., Hedgecock, I. M., 510 Corbitt, E. S. and Sunderland, E. M.: Observational and modelling constraints on global anthropogenic enrichment of mercury, Environ. Sci. Technol., 49(7), 4036–4047, doi:10.1021/es5058665, 2015.
- An, J., Zhang, L., Lu, X., Pelletier, D. A., Pierce, E. M., Johs, A., Parks, J. M. and Gu, B.: Mercury Uptake by Desulfovibrio desulfuricans ND132: Passive or Active?, Environ. Sci. Technol., 53(11), 6264–6272, doi:10.1021/acs.est.9b00047, 2019.

- Andersson, M. E., Gårdfeldt, K., Wängberg, I., Sprovieri, F., Pirrone, N. and Lindqvist, O.: Reprint of “Seasonal and daily  
515 variation of mercury evasion at coastal and off shore sites from the Mediterranean Sea,” *Mar. Chem.*, 107(1), 104–116,  
doi:10.1016/j.marchem.2007.06.020, 2007.
- Baya, P. A., Gosselin, M., Lehnher, I., St. Louis, V. L. and Hintelmann, H.: Determination of monomethylmercury and  
dimethylmercury in the arctic marine boundary layer, *Environ. Sci. Technol.*, doi:10.1021/es502601z, 2015.
- Blum, J. D., Popp, B. N., Drazen, J. C., Anela Choy, C. and Johnson, M. W.: Methylmercury production below the mixed  
520 layer in the North Pacific Ocean, *Nat. Geosci.*, 6(10), 879–884, doi:10.1038/ngeo1918, 2013.
- Bowman, K. L., Hammerschmidt, C. R., Lamborg, C. H. and Swarr, G.: Mercury in the North Atlantic Ocean: The U.S.  
GEOTRACES zonal and meridional sections, *Deep. Res. Part II Top. Stud. Oceanogr.*, 116, 251–261,  
doi:10.1016/j.dsr2.2014.07.004, 2015.
- Bowman, K. L., Hammerschmidt, C. R., Lamborg, C. H., Swarr, G. J. and Agather, A. M.: Distribution of mercury species  
525 across a zonal section of the eastern tropical South Pacific Ocean (U.S. GEOTRACES GP16), *Mar. Chem.*, 186, 156–166,  
doi:10.1016/j.marchem.2016.09.005, 2016.
- Bowman, K. L., Lamborg, C. H. and Agather, A. M.: A global perspective on mercury cycling in the ocean, *Sci. Total Environ.*,  
710, 136166, doi:10.1016/j.scitotenv.2019.136166, 2020.
- [Bosc, E., Bricaud, A., and Antoine, D.: Seasonal and interannual variability in algal biomass and primary production in the  
530 Mediterranean Sea, as derived from 4 years of SeaWiFS observations, \*Global Biogeochem. Cycles\*, 18, n/a-n/a,  
<https://doi.org/10.1029/2003GB002034>, 2004.](https://doi.org/10.1029/2003GB002034)
- [Bricaud, A., Bosc, E., and Antoine, D.: Algal biomass and sea surface temperature in the Mediterranean Basin Intercomparison  
of data from various satellite sensors, and implications for primary production estimates, \*Remote Sens. Environ.\*, 81, 163–178,  
\[https://doi.org/10.1016/S0034-4257\\(01\\)00335-2\]\(https://doi.org/10.1016/S0034-4257\(01\)00335-2\), 2002.](https://doi.org/10.1016/S0034-4257(01)00335-2)
- Cael, B. B., Cavan, E. L. and Britten, G. L.: Reconciling the Size-Dependence of Marine Particle Sinking Speed, *Geophys.  
535 Res. Lett.*, 48(5), 1–11, doi:10.1029/2020GL091771, 2021.
- Canu, D. and Rosati, G.: Long-term scenarios of mercury budgeting and exports for a Mediterranean hot spot (Marano-Grado  
Lagoon, Adriatic Sea), *Estuar. Coast. Shelf Sci.*, 198, 518–528, doi:10.1016/j.ecss.2016.12.005, 2017.
- Canu, D., Ghermandi, A., Nunes, P. A. L. D., Lazzari, P., Cossarini, G. and Solidoro, C.: Estimating the value of carbon  
540 sequestration ecosystem services in the mediterranean sea: An ecological economics approach, *Glob. Environ. Chang.*, 32,  
87–95, doi:10.1016/j.gloenvcha.2015.02.008, 2015.
- Canu, D. M., Rosati, G. and Solidoro, C.: Mercury Budget and Scenario Analysis for the Marano-Grado Lagoon, Using  
Modelling and Observations, *Proc.*, 30(1), doi:10.3390/proceedings2019030019, 2019.
- Choe, K.-Y. and Gill, G. a.: Distribution of particulate, colloidal, and dissolved mercury in San Francisco Bay estuary. 2.  
545 Monomethyl mercury, *Limnol. Oceanogr.*, 48(4), 1547–1556, doi:10.4319/lo.2003.48.4.1547, 2003.
- Choe, K.-Y., Gill, G. A. and Lehman, R.: Distribution of particulate, colloidal, and dissolved mercury in San Francisco Bay  
estuary. 1. Total mercury, *Limnol. Oceanogr.*, 48(4), 1535–1546, doi:10.4319/lo.2003.48.4.1547, 2003.

- Cinnirella, S., Bruno, D. E., Pirrone, N., Horvat, M., Živković, I., Evers, D. C., Johnson, S. and Sunderland, E. M.: Mercury concentrations in biota in the Mediterranean Sea, a compilation of 40 years of surveys, *Sci. data*, 6(1), 205, doi:10.1038/s41597-019-0219-y, 2019.
- 550 Coale, K. H., Heim, W. A., Negrey, J., Weiss-Penzias, P., Fernandez, D., Olson, A., Chiswell, H., Byington, A., Bonnema, A., Martenuk, S., Newman, A., Beebe, C. and Till, C.: The distribution and speciation of mercury in the California current: Implications for mercury transport via fog to land, *Deep. Res. Part II Top. Stud. Oceanogr.*, 151(May), 77–88, doi:10.1016/j.dsr2.2018.05.012, 2018.
- 555 Conaway, C. H., Black, F. J., Gault-Ringold, M., Pennington, J. T., Chavez, F. P. and Flegal, A. R.: Dimethylmercury in coastal upwelling waters, Monterey Bay, California, *Environ. Sci. Technol.*, 43(5), 1305–1309, doi:10.1021/es802705t, 2009.
- Cossa, D. and Coquery, M.: The Mediterranean Mercury Anomaly, a Geochemical or a Biological Issue, in *The Mediterranean Sea*, edited by A. Saliot, pp. 177–208, Springer Berlin Heidelberg, Berlin, Heidelberg., 2005.
- Cossa, D., Averty, B. and Pirrone, N.: The origin of methylmercury in open Mediterranean waters, *Limnol. Oceanogr.*, 54(3), 837–844, doi:10.4319/lo.2009.54.3.0837, 2009.
- 560 Cossa, D., Harmelin-Vivien, M., Mellon-Duval, C., Loizeau, V., Averty, B., Crochet, S., Chou, L. and Cadiou, J.-F.: Influences of bioavailability, trophic position, and growth on methylmercury in hakes (*Merluccius merluccius*) from Northwestern Mediterranean and Northeastern Atlantic., *Environ. Sci. Technol.*, 46(9), 4885–93, doi:10.1021/es204269w, 2012.
- Cossa, D., Durrieu de Madron, X., Schäfer, J., Lancelleur, L., Guédron, S., Buscaill, R., Thomas, B., Castelle, S. and Naudin, J.-J.: The open sea as the main source of methylmercury in the water column of the Gulf of Lions (Northwestern Mediterranean margin), *Geochim. Cosmochim. Acta*, 199, 222–237, doi:10.1016/j.gca.2016.11.037, 2017.
- [Cossa, D., Knoery, J., Bănaru, D., Harmelin-Vivien, M., Sonke, J. E., Hedgecock, I. M., Bravo, A. G., Rosati, G., Canu, D., Horvat, M., Sprovieri, F., Pirrone, N., and Heimbürger-Boavida, L.-E.: Mediterranean Mercury Assessment 2022: An Updated Budget, Health Consequences, and Research Perspectives, \*Environ. Sci. Technol.\*, 56, 3840–3862, <https://doi.org/10.1021/acs.est.1c03044>, 2022.](#)
- 570 [Cossarini, G., Lazzari, P., and Solidoro, C.: Spatiotemporal variability of alkalinity in the Mediterranean Sea, 12, 1647–1658, <https://doi.org/10.5194/bg-12-1647-2015>, 2015.](#)
- [Cossarini, G., Feudale, L., Teruzzi, A., Bolzon, G., Coideasa, G., Solidoro, C., Di Biagio, V., Amadio, C., Lazzari, P., Brosich, A., and Salon, S.: High-Resolution Reanalysis of the Mediterranean Sea Biogeochemistry \(1999–2019\), \*Front. Mar. Sci.\*, 8, 1–21, <https://doi.org/10.3389/fmars.2021.741486>, 2021.](#)
- 575 [Crise, A., Allen, J. I., Baretta, J., Crispi, G., Mosetti, R., and Solidoro, C.: The Mediterranean pelagic ecosystem response to physical forcing, \*Prog. Oceanogr.\*, 44, 219–243, \[https://doi.org/10.1016/S0079-6611\\(99\\)00027-0\]\(https://doi.org/10.1016/S0079-6611\(99\)00027-0\), 1999.](#)
- [Crispi, G., Mosetti, R., Solidoro, C., and Crise, A.: Nutrients cycling in Mediterranean basins: The role of the biological pump in the trophic regime, \*Ecol. Modell.\*, 138, 101–114, \[https://doi.org/10.1016/S0304-3800\\(00\\)00396-3\]\(https://doi.org/10.1016/S0304-3800\(00\)00396-3\), 2001.](#)
- 580 [variability in the Mediterranean Sea ecosystem: Insight from a coupled model, \*J. Mar. Syst.\*, 197, 103176, <https://doi.org/10.1016/j.jmarsys.2019.05.002>, 2019.](#)

ha formattato: Inglese (Stati Uniti)

Di Biagio, V., Cossarini, G., Salon, S., and Solidoro, C.: Extreme event waves in marine ecosystems: An application to Mediterranean Sea surface chlorophyll, *17*, 5967–5988, <https://doi.org/10.5194/bg-17-5967-2020>, 2020.

D’Ortenzio, F., D’Alcalà, M.R., 2009. On the trophic regimes of the Mediterranean Sea: A satellite analysis. *Biogeosciences* 6, 139–148. <https://doi.org/10.5194/bg-6-139-2009>

Fantozzi, L., Manca, G., Ammoscato, I., Pirrone, N. and Sprovieri, F.: The cycling and sea-air exchange of mercury in the waters of the Eastern Mediterranean during the 2010 MED-OCEANOR cruise campaign, *Sci. Total Environ.*, 448, 151–162, doi:10.1016/j.scitotenv.2012.09.062, 2013.

Ferrara, R., Ceccarini, C., Lanzillotta, E., Gårdfeldt, K., Sommar, J., Horvat, M., Logar, M., Fajon, V. and Kotnik, J.: Profiles of dissolved gaseous mercury concentration in the Mediterranean seawater, *Atmos. Environ.*, 37(SUPPL. 1), 85–92, doi:10.1016/S1352-2310(03)00248-6, 2003.

Gårdfeldt, K., Sommar, J., Ferrara, R., Ceccarini, C., Lanzillotta, E., Munthe, J., Wängberg, I., Lindqvist, O., Pirrone, N., Sprovieri, F., Pesenti, E. and Strömberg, D.: Evasion of mercury from coastal and open waters of the Atlantic Ocean and the Mediterranean Sea, *Atmos. Environ.*, 37, 73–84, doi:10.1016/S1352-2310(03)00238-3, 2003.

Gencarelli, C. N., De Simone, F., Hedgecock, I. M., Sprovieri, F., and Pirrone, N.: Development and application of a regional-scale atmospheric mercury model based on WRF/Chem: A Mediterranean area investigation, *Environ. Sci. Pollut. Res.*, 21, 4095–4109, <https://doi.org/10.1007/s11356-013-2162-3>, 2014.

Gosnell, K. J. and Mason, R. P.: Mercury and methylmercury incidence and bioaccumulation in plankton from the central Pacific Ocean, *Mar. Chem.*, 177, 772–780, doi:10.1016/j.marchem.2015.07.005, 2015.

Gosnell, K. J., Balcom, P. H., Tobias, C. R., Gilhooly, W. P. and Mason, R. P.: Spatial and temporal trophic transfer dynamics of mercury and methylmercury into zooplankton and phytoplankton of Long Island Sound, *Limnol. Oceanogr.*, 62(3), 1122–1138, doi:10.1002/lno.10490, 2017.

Hammerschmidt, C. R., Finiguerra, M. B., Weller, R. L. and Fitzgerald, W. F.: Methylmercury Accumulation in Plankton on the Continental Margin of the Northwest Atlantic Ocean, *Environ. Sci. Technol.*, 47, 3671–3677, 2013.

Harding, G., Dalziel, J. and Vass, P.: Bioaccumulation of methylmercury within the marine food web of the outer Bay of Fundy, Gulf of Maine, *PLoS One*, 13(7), 1–30, doi:10.1371/journal.pone.0197220, 2018.

Harmelin-Vivien, M., Cossa, D., Crochet, S., Bănar, D., Letourneur, Y. and Mellon-Duval, C.: Difference of mercury bioaccumulation in red mullets from the north-western Mediterranean and Black seas, *Mar. Pollut. Bull.*, 58(5), 679–685, doi:10.1016/j.marpolbul.2009.01.004, 2009.

Heimbürger, L.-E., Cossa, D., Marty, J.-C., Migon, C., Averty, B., Dufour, A. and Ras, J.: Methylmercury distributions in relation to the presence of nano- and picophytoplankton in an oceanic water column (Ligurian Sea, North-western Mediterranean), *Geochim. Cosmochim. Acta*, 74(19), 5549–5559, doi:10.1016/j.gca.2010.06.036, 2010.

Hines, M. E., Horvat, M., Faganeli, J., Bonzongo, J. C. J., Barkay, T., Major, E. B., Scott, K. J., Bailey, E. A., Warwick, J. J. and Lyons, W. B.: Mercury biogeochemistry in the Idrija River, Slovenia, from above the mine into the Gulf of Trieste, *Environ. Res.*, 83(2), 129–139, doi:10.1006/enrs.2000.4052, 2000.

- Horvat, M., Covelli, S., Faganeli, J., Logar, M., Mandić, V., Rajar, R., Širca, A. and Žagar, D.: Mercury in contaminated coastal environments; a case study: The Gulf of Trieste, *Sci. Total Environ.*, 237–238, 43–56, doi:10.1016/S0048-9697(99)00123-0, 1999.
- 620 Horvat, M., Kotnik, J., Logar, M., Fajon, V., Zvonarić, T. and Pirrone, N.: Speciation of mercury in surface and deep-sea waters in the Mediterranean Sea, *Atmos. Environ.*, 37, Supple(0), 93–108, doi:http://dx.doi.org/10.1016/S1352-2310(03)00249-8, 2003.
- Horvat, M., Degenek, N., Lipej, L., Snoj Tratnik, J. and Faganeli, J.: Trophic transfer and accumulation of mercury in ray species in coastal waters affected by historic mercury mining (Gulf of Trieste, northern Adriatic Sea), *Environ. Sci. Pollut. Res.*, 21(6), 4163–4176, doi:10.1007/s11356-013-2262-0, 2014.
- 625 [Jiskra, M., Heimbürger-Boavida, L.-E., Desgranges, M.-M., Petrova, M. V., Dufour, A., Ferreira-Araujo, B., Masbou, J., Chmeleff, J., Thyssen, M., Point, D., and Sonke, J. E.: Mercury stable isotopes constrain atmospheric sources to the ocean, \*Nature\*, 597, 678–682, <https://doi.org/10.1038/s41586-021-03859-8>, 2021.](#)
- Jonsson, S., Mazrui, N. M. and Mason, R. P.: Dimethylmercury Formation Mediated by Inorganic and Organic Reduced Sulfur Surfaces, *Sci. Rep.*, 6(August), 27958, doi:10.1038/srep27958, 2016.
- 630 Jørgensen, S. E., Friis, M. B., Henriksen, J., Jørgensen, L. A. and Mejer, H. F.: Handbook of Environmental Data and Ecological Parameters, edited by S. E. Jørgensen, Pergamon Press, International Society for Ecological Modelling., 1979.
- Kotnik, J., Horvat, M., Tessier, E., Ogrinc, N., Monperrus, M., Amouroux, D., Fajon, V., Gibičar, D., Žižek, S., Sprovieri, F. and Pirrone, N.: Mercury speciation in surface and deep waters of the Mediterranean Sea, *Mar. Chem.*, 107(1), 13–30, doi:10.1016/j.marchem.2007.02.012, 2007.
- 635 Kotnik, J., Horvat, M., Ogrinc, N., Fajon, V., Žagar, D., Cossa, D., Sprovieri, F. and Pirrone, N.: Mercury speciation in the Adriatic Sea, *Mar. Pollut. Bull.*, 96(1–2), 136–148, doi:10.1016/j.marpolbul.2015.05.037, 2015.
- Lamborg, C. H., Hammerschmidt, C. R., Bowman, K. L., Swarr, G. J., Munson, K. M., Ohnemus, D. C., Lam, P. J., Heimbürger, L.-E., Rijkenberg, M. J. A. and Saito, M. A.: A global ocean inventory of anthropogenic mercury based on water column measurements, *Nature*, 512(7512), 65–68, doi:10.1038/nature13563, 2014.
- 640 Lamborg, C. H., Hammerschmidt, C. R. and Bowman, K. L.: An examination of the role of particles in oceanic mercury cycling, *Philos. Trans. R. Soc. A Math. Phys. Eng. Sci.*, 374(2081), 20150297, doi:10.1098/rsta.2015.0297, 2016.
- Lanzillotta, E., Ceccarini, C. and Ferrara, R.: Photo-induced formation of dissolved gaseous mercury in coastal and offshore seawater of the Mediterranean basin, *Sci. Total Environ.*, 300(1–3), 179–187, doi:10.1016/S0048-9697(02)00223-1, 2002.
- Lazzari, P., Teruzzi, A., Salon, S., Campagna, S., Calonaci, C., Colella, S., Tonani, M. and Crise, A.: Pre-operational short-term forecasts for Mediterranean Sea biogeochemistry, *Ocean Sci.*, 6(1), 25–39, doi:10.5194/os-6-25-2010, 2010.
- 645 Lazzari, P., Solidoro, C., Ibello, V., Salon, S., Teruzzi, A., Béranger, K., Colella, S. and Crise, A.: Seasonal and inter-annual variability of plankton chlorophyll and primary production in the Mediterranean Sea: A modelling approach, *Biogeosciences*, 9(1), 217–233, doi:10.5194/bg-9-217-2012, 2012.

- Lazzari, P., Mattia, G., Solidoro, C., Salon, S., Crise, A., Zavatarelli, M., Oddo, P. and Vichi, M.: The impacts of climate change and environmental management policies on the trophic regimes in the Mediterranean Sea: Scenario analyses, *J. Mar. Syst.*, 135, 137–149, doi:10.1016/j.jmarsys.2013.06.005, 2014.
- Lazzari, P., Solidoro, C., Salon, S. and Bolzon, G.: Spatial variability of phosphate and nitrate in the Mediterranean Sea: A modelling approach, *Deep. Res. Part I Oceanogr. Res. Pap.*, 108(January), 39–52, doi:10.1016/j.dsr.2015.12.006, 2016.
- Lazzari, P., Álvarez, E., Terzić, E., Cossarini, G., Chernov, I., D’ortenzio, F. and Organelli, E.: Cdom spatiotemporal variability in the mediterranean sea: A modelling study, *J. Mar. Sci. Eng.*, 9(2), 1–18, doi:10.3390/jmse9020176, 2021.
- Lee, C. and Fisher, N. S.: Methylmercury uptake by diverse marine phytoplankton, *Limnol. Oceanogr.*, 61, 1626–1639, doi:10.1002/lno.10318, 2016.
- Lehnherr, I., St. Louis, V. L., Hintelmann, H. and Kirk, J. L.: Methylation of inorganic mercury in polar marine waters, *Nat. Geosci.*, 4(April), 298–302, doi:10.1038/ngeo1134, 2011.
- 660 [Liu, M., Zhang, Q., Maavara, T., Liu, S., Wang, X., and Raymond, P. A.: Rivers as the largest source of mercury to coastal oceans worldwide, \*Nat. Geosci.\*, <https://doi.org/10.1038/s41561-021-00793-2>, 2021.](https://doi.org/10.1038/s41561-021-00793-2)
- Luo, H., Cheng, Q. and Pan, X.: Photochemical behaviors of mercury (Hg) species in aquatic systems: A systematic review on reaction process, mechanism, and influencing factor, *Sci. Total Environ.*, 720, 137540, doi:10.1016/j.scitotenv.2020.137540, 2020.
- 665 Mahlmann, D. M., Jahnke, J. and Loosen, P.: Rapid determination of the dry weight of single, living cyanobacterial cells using the Mach-Zehnder double-beam interference microscope, *Eur. J. Phycol.*, 43(4), 355–364, doi:10.1080/09670260802168625, 2008.
- Margirier, F., Testor, P., Heslop, E., Mallil, K., Bosse, A., Houpert, L., Mortier, L., Bouin, M. N., Coppola, L., D’Ortenzio, F., Durrieu de Madron, X., Mourre, B., Prieur, L., Raimbault, P. and Taillandier, V.: Abrupt warming and salinification of intermediate waters interplays with decline of deep convection in the Northwestern Mediterranean Sea, *Sci. Rep.*, 10(1), 1–11, doi:10.1038/s41598-020-77859-5, 2020.
- 670 Mason, R. P., Choi, A. L., Fitzgerald, W. F., Hammerschmidt, C. R., Lamborg, C. H., Soerensen, A. L. and Sunderland, E. M.: Mercury biogeochemical cycling in the ocean and policy implications, *Environ. Res.*, 119, 101–117, doi:10.1016/j.envres.2012.03.013, 2012.
- 675 McGeer, J. C., Brix, K. V., Skeaff, J. M., Deforest, D. K., Brigham, S. I., Adams, W. J. and Green, A.: Inverse relationship between bioconcentration factor and exposure concentration for metals: Implications for hazard assessment of metals in the aquatic environment, *Environ. Toxicol. Chem.*, 22(5), 1017–1037, doi:10.1897/1551-5028(2003)022<1017:IRBBFA>2.0.CO;2, 2003.
- Melaku Canu, D., Rosati, G., Solidoro, C., Heimbürger, L.-E. and Acquavita, A.: A comprehensive assessment of the mercury budget in the Marano–Grado Lagoon (Adriatic Sea) using a combined observational modeling approach, *Mar. Chem.*, 177, 742–752, doi:10.1016/j.marchem.2015.10.013, 2015.
- 680

- Mihanović, H., Vilibić, I., Šepić, J., Matic, F., Ljubešić, Z., Mauri, E., Gerin, R., Notarstefano, G. and Poulain, P. M.: Observation, Preconditioning and Recurrence of Exceptionally High Salinities in the Adriatic Sea, *Front. Mar. Sci.*, 8(July), 1–22, doi:10.3389/fmars.2021.672210, 2021.
- 685 Monperrus, M., Tessier, E., Amouroux, D., Leynaert, A., Huonnic, P. and Donard, O. F. X.: Mercury methylation, demethylation and reduction rates in coastal and marine surface waters of the Mediterranean Sea, *Mar. Chem.*, 107(1), 49–63, doi:10.1016/j.marchem.2007.01.018, 2007.
- Motta, L. C., Blum, J. D., Johnson, M. W., Umhau, B. P., Popp, B. N., Washburn, S. J., Drazen, J. C., Benitez-Nelson, C. R., Hannides, C. C. S., Close, H. G. and Lamborg, C. H.: Mercury Cycling in the North Pacific Subtropical Gyre as Revealed by
- 690 Mercury Stable Isotope Ratios, *Global Biogeochem. Cycles*, 33(6), 777–794, doi:10.1029/2018GB006057, 2019.
- Munson, K. M., Lamborg, C., Swarr, G. J. and Saito, M. A.: Mercury species concentrations and fluxes in the Central Tropical Pacific Ocean, *Global Biogeochem. Cycles*, 29(Ii), 656–676, doi:10.1002/2015GB005120. Received, 2015.
- Munson, K. M., Lamborg, C. H., Boiteau, R. M. and Saito, M. A.: Dynamic mercury methylation and demethylation in oligotrophic marine water, *Biogeosciences*, 15(21), 6451–6460, doi:10.5194/bg-15-6451-2018, 2018.
- 695 Nerentorp Mastromonaco, M. G., Gårdfeldt, K. and Wängberg, I.: Seasonal and spatial evasion of mercury from the western Mediterranean Sea, *Mar. Chem.*, 193, 34–43, doi:10.1016/j.marchem.2017.02.003, 2017.
- Nightingale, P. D., Malin, G., Law, C. S., Watson, A. J., Liss, P. S., Liddicoat, M. I., Boutin, J. and Upstill-Goddard, R. C.: In situ evaluation of air-sea gas exchange parameterizations using novel conservative and volatile tracers, *Global Biogeochem. Cycles*, 14(1), 373–387, doi:10.1029/1999GB900091, 2000.
- 700 Ortiz, V. L., Mason, R. P. and Evan Ward, J.: An examination of the factors influencing mercury and methylmercury particulate distributions, methylation and demethylation rates in laboratory-generated marine snow, *Mar. Chem.*, 177, 753–762, doi:10.1016/j.marchem.2015.07.006, 2015.
- [Palanques, A., Guillén, J., Puig, P., and Grimalt, J. O.: Effects of flushing flows on the transport of mercury-polluted particulate matter from the Flix Reservoir to the Ebro Estuary, \*J. Environ. Manage.\*, 260, <https://doi.org/10.1016/j.jenvman.2019.110028>, 2020.](https://doi.org/10.1016/j.jenvman.2019.110028)
- 705 [Panagos, P., Jiskra, M., Borrelli, P., Liakos, L., and Ballabio, C.: Mercury in European topsoils: Anthropogenic sources, stocks and fluxes, \*Environ. Res.\*, 201, 111556, <https://doi.org/10.1016/j.envres.2021.111556>, 2021.](https://doi.org/10.1016/j.envres.2021.111556)
- [Pinardi, N. and Masetti, E.: Variability of the large scale general circulation of the Mediterranean Sea from observations and modelling: A review, \*Palaeogeogr. Palaeoclimatol. Palaeoecol.\*, 158, 153–173, \[https://doi.org/10.1016/S0031-0182\\(00\\)00048-1\]\(https://doi.org/10.1016/S0031-0182\(00\)00048-1\), 2000.](https://doi.org/10.1016/S0031-0182(00)00048-1)
- 710 [Pinardi, N., Zavatarelli, M., Adani, M., Coppini, G., Fratianni, C., Oddo, P., Simoncelli, S., Tonani, M., Lyubartsev, V., Dobricic, S., and Bonaduce, A.: Mediterranean Sea large-scale low-frequency ocean variability and water mass formation rates from 1987 to 2007: A retrospective analysis, \*Prog. Oceanogr.\*, 132, 318–332, <https://doi.org/10.1016/j.pocean.2013.11.003>, 2015.](https://doi.org/10.1016/j.pocean.2013.11.003)

- 715 [Ramondenc, S., Lombard, F., Santinelli, C., Stemann, L., Gorsky, G., and Guidi, L.: An initial carbon export assessment in the Mediterranean Sea based on drifting sediment traps and the Underwater Vision Profiler data sets, \*Deep. Res. Part I\*, 117, 107–119, <https://doi.org/10.1016/j.dsr.2016.08.015>, 2016.](#)
- Rimondi, V., Costagliola, P., Lattanzi, P., Morelli, G., Cara, G., Cencetti, C., Fagotti, C., Fredduzzi, A., Marchetti, G., Sconocchia, A. and Torricelli, S.: A 200 km-long mercury contamination of the Paglia and Tiber floodplain: Monitoring results and implications for environmental management, *Environ. Pollut.*, 255, 113191, doi:10.1016/j.envpol.2019.113191, 2019.
- 720 Rosati, G., Heimbürger, L. E., Melaku Canu, D., Lagane, C., Laffont, L., Rijkenberg, M. J. A., Gerringa, L. J. A., Solidoro, C., Gencarelli, C. N., Hedgecock, I. M., De Baar, H. J. W. and Sonke, J. E.: Mercury in the Black Sea: new insights from measurements and numerical modeling, *Global Biogeochem. Cycles*, 32(4), 1–22, doi:10.1002/2017GB005700, 2018.
- Rosati, G., Solidoro, C. and Canu, D.: Mercury dynamics in a changing coastal area over industrial and postindustrial phases: Lessons from the Venice Lagoon, *Sci. Total Environ.*, 743(July), 1–15, doi:10.1016/j.scitotenv.2020.140586, 2020.
- 725 Rosati, G., Canu, D., Lazzari, P. and Solidoro, C.: OGSTM-BFM-Hg model code. Zenodo. doi:10.5281/zenodo.5851442, 2022.
- Rosati, G., Laurent, C., Solidoro, C. and Canu, D.: Developing a model for mercury cycling in coastal areas. in prep.
- Salon, S., Cossarini, G., Bolzon, G., Feudale, L., Lazzari, P., Teruzzi, A., Solidoro, C. and Crise, A.: Novel metrics based on biogeochemical argo data to improve the model uncertainty evaluation of the cmems mediterranean marine ecosystem forecasts, *Ocean Sci.*, 15(4), 997–1022, doi:10.5194/os-15-997-2019, 2019.
- 730 Schaefer, J. K. and Morel, F. M. M.: High methylation rates of mercury bound to cysteine by *Geobacter sulfurreducens*, *Nat. Geosci.*, 2(2), 123–126, 2009.
- Schartup, A. T., Ndu, U., Balcom, P. H., Mason, R. P. and Sunderland, E. M.: Contrasting effects of marine and terrestrially derived dissolved organic matter on mercury speciation and bioavailability in seawater, *Environ. Sci. Technol.*, 49(10), 5965–5972, doi:10.1021/es506274x, 2015.
- 735 Schartup, A. T., Qureshi, A., Dassuncao, C., Thackray, C. P., Harding, G. and Sunderland, E. M.: A Model for Methylmercury Uptake and Trophic Transfer by Marine Plankton, *Environ. Sci. Technol.*, 52(2), 654–662, doi:10.1021/acs.est.7b03821, 2018.
- Schlitzer, R.: Ocean Data View, [online] Available from: <http://odv.awi.de>, 2014.
- 740 De Simone, F., Gencarelli, C. N., Hedgecock, I. M. and Pirrone, N.: Global atmospheric cycle of mercury: a model study on the impact of oxidation mechanisms, *Environ. Sci. Pollut. Res.*, 21(6), 4110–4123, doi:10.1007/s11356-013-2451-x, 2014.
- Sonke, J. E., Heimbürger, L. E. and Dommergue, A.: Mercury biogeochemistry: Paradigm shifts, outstanding issues and research needs, *Comptes Rendus - Geosci.*, 345(5–6), 213–224, doi:10.1016/j.crte.2013.05.002, 2013.
- Sunderland, E. M., Krabbenhoft, D. P., Moreau, J. W., Strode, S. A. and Landing, W. M.: Mercury sources, distribution, and bioavailability in the North Pacific Ocean: Insights from data and models, *Global Biogeochem. Cycles*, 23(2), 1–14, doi:10.1029/2008GB003425, 2009.
- 745



- Terzić, E., Lazzari, P., Organelli, E., Solidoro, C., Salon, S., D'Ortenzio, F. and Conan, P.: Merging bio-optical data from Biogeochemical-Argo floats and models in marine biogeochemistry, *Biogeosciences*, 16(12), 2527–2542, doi:10.5194/bg-16-2527-2019, 2019.
- 750 Tseng, C. M., Ang, S. J., Chen, Y. S., Shiao, J. C., Lamborg, C. H., He, X. and Reinfelder, J. R.: Bluefin tuna reveal global patterns of mercury pollution and bioavailability in the world's oceans, *Proc. Natl. Acad. Sci. U. S. A.*, 118(38), 1–6, doi:10.1073/pnas.2111205118, 2021.
- UNEP: Global mercury assessment 2018, Geneva, Switzerland. [online] Available from: <http://www.chem.unep.ch/mercury/report/GMA-report-TOC.htm%5Cnhttp://www.chem.unep.ch/MERCURY/Report/revdraft-afterWG/assessment-report-4Oct02.pdf>, 2019.
- 755 Vichi, M., Lovato, T., Lazzari, P., Cossarini, G., Gutierrez Mlot, E., Mattia, G., Masina, S., McKiver, W., Pinardi, N., Solidoro, C., Tedesco, L. and Zavattelli, M.: The Biogeochemical Flux Model (BFM) Equation Description and User Manual, , 5(August), 1–104, 2015.
- Vignati, D. A. L., Burdino, E., Congiu, A. M., Cicala, F., Pardos, M., Nieddu, G. F. and Ugazio, G.: Quality evaluation of sediments from 24 tributaries of the Po River, Italy, *Water. Air. Soil Pollut.*, 190(1–4), 129–141, doi:10.1007/s11270-007-9586-7, 2008.
- 760 Wang, K., Munson, K. M., Armstrong, D. A., Macdonald, R. W. and Wang, F.: Determining seawater mercury methylation and demethylation rates by the seawater incubation approach: A critique, *Mar. Chem.*, 219(January), 103753, doi:10.1016/j.marchem.2020.103753, 2020.
- 765 Wu, P., Zakem, E. J., Dutkiewicz, S. and Zhang, Y.: Biomagnification of Methylmercury in a Marine Plankton Ecosystem, *Environ. Sci. Technol.*, 54, 5446–5455, doi:10.1021/acs.est.9b06075, 2020.
- Wu, P., Dutkiewicz, S., Monier, E. and Zhang, Y.: Bottom-Heavy Trophic Pyramids Impair Methylmercury Biomagnification in the Marine Plankton Ecosystems, *Environ. Sci. Technol.*, 55(22), 15476–15483, doi:10.1021/acs.est.1c04083, 2021.
- Žagar, D., Petkovšek, G., Rajar, R., Sirknik, N., Horvat, M., Voudouri, A., Kallos, G. and Četina, M.: Modelling of mercury transport and transformations in the water compartment of the Mediterranean Sea, *Mar. Chem.*, 107(1), 64–88, doi:10.1016/j.marchem.2007.02.007, 2007.
- 770 Žagar, D., Sirknik, N., Četina, M., Horvat, M., Kotnik, J., Ogrinc, N., Hedgecock, I. M., Cinnirella, S., Pirrone, Nicola, De Simone, F. and Gencarelli, C. N.: Mercury in the Mediterranean. Part 2: Processes and mass balance, *Environ. Sci. Pollut. Res.*, 21(6), 4081–4094, doi:10.1007/s11356-013-2055-5, 2014.
- 775 Zhang, C., Dang, H., Azam, F., Benner, R., Legendre, L., Passow, U., Polimene, L., Robinson, C., Suttle, C. A. and Jiao, N.: Evolving paradigms in biological carbon cycling in the ocean, *Natl. Sci. Rev.*, 5(4), 481–499, doi:10.1093/nsr/nwy074, 2018.
- Zhang, L., Wu, S., Zhao, L., Lu, X., Pierce, E. M. and Gu, B.: Mercury Sorption and Desorption on Organo-Mineral Particulates as a Source for Microbial Methylation, *Environ. Sci. Technol.*, 53(5), 2426–2433, doi:10.1021/acs.est.8b06020, 2019.

780 Zhang, Y., Jaeglé, L. and Thompson, L.: Natural biogeochemical cycle of mercury in a global three-dimensional ocean tracer model, *Global Biogeochem. Cycles*, 28, 553–570, doi:10.1002/2014GB004814, 2014a.

Zhang, Y., Jaeglé, L., Thompson, L. A. and Streets, D. G.: Six centuries of changing oceanic mercury, *Global Biogeochem. Cycles*, 28(11), 1251–1261, doi:10.1002/2014GB004939, 2014b.

Zhang, Y., Soerensen, A. L., Schartup, A. T. and Sunderland, E. M.: A global model for methylmercury formation and uptake at the base of marine food webs, *Global Biogeochem. Cycles*, 1–21, doi:10.1029/2019GB006348, 2020.

785

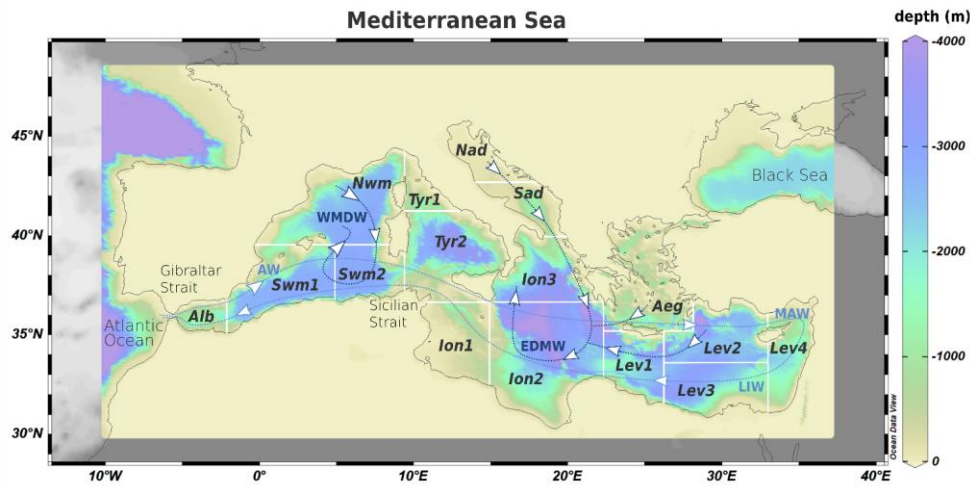


Figure 1: Bathymetric map of the Mediterranean Sea (from Ocean Data View, Schlitzer, 2014). The white contours indicate the subdivision of the model domain in subbasins: Alboran Sea (*Alb*), Southwest western Mediterranean (*Swm1* and *Swm2*), Northwestern Mediterranean (*Nwm*), Tyrrhenian Sea (*Tyr1* and *Tyr2*), northern Adriatic Sea (*Nad*), southern Adriatic Sea (*Sad*), Ionian Sea (*Ion1*, *Ion2*, and *Ion3*), Aegean Sea (*Aeg*), and Levantine basin (*Lev1*, *Lev2*, *Lev3*, and *Lev4*). The light blue line shows the zonal cell driven by the surface inflow of Atlantic Water inflow (*AW*) that moves eastward forming Modified Atlantic Water (*MAW*) and Levantine Intermediate Water (*LIW*), outflowing at intermediate depths at the Gibraltar Strait. The dark blue lines show the path of meridional cells related to winter convection in the *Nwm*, *Nad*, *Sad*, *Aeg*, and *Lev* originating the Western and Eastern Mediterranean Deep Water (*WMDW* and *EMDW*).

790

795

- ha formattato: Tipo di carattere: Corsivo
- ha formattato: Tipo di carattere: Corsivo
- ha formattato: Tipo di carattere: Corsivo
- ha formattato: Tipo di carattere: Corsivo
- ha formattato: Tipo di carattere: Corsivo
- ha formattato: Tipo di carattere: Corsivo
- ha formattato: Tipo di carattere: Corsivo
- ha formattato: Tipo di carattere: Corsivo
- ha formattato: Tipo di carattere: Corsivo
- ha formattato: Tipo di carattere: Corsivo
- ha formattato: Tipo di carattere: Corsivo
- ha formattato: Tipo di carattere: Corsivo
- ha formattato: Tipo di carattere: Corsivo
- ha formattato: Tipo di carattere: Corsivo
- ha formattato: Tipo di carattere: Corsivo

## OGSTM-BFM-MERC model coupling scheme

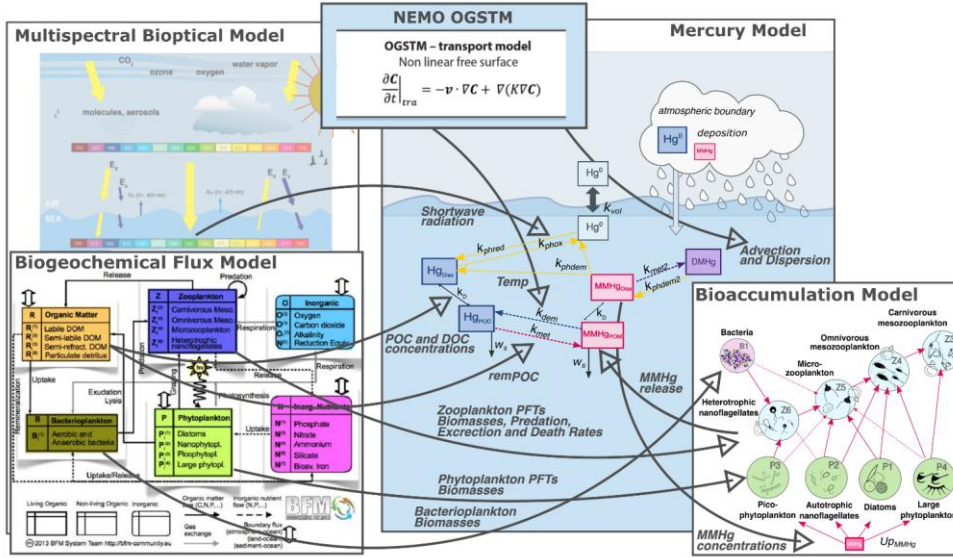


Figure 2: Overview of the coupling in the OGSTM-BFM-Hg model, which integrates the biogeochemistry and bioaccumulation of Hg species in the OGSTM-BFM model, previously coupled to the transport model NEMO (Salon et al., 2019) and to a multispectral biophysical model (Lazzari et al., 2021). The thick grey arrows with text highlight variables and fluxes read by the Hg biogeochemical model (Fig. 3).

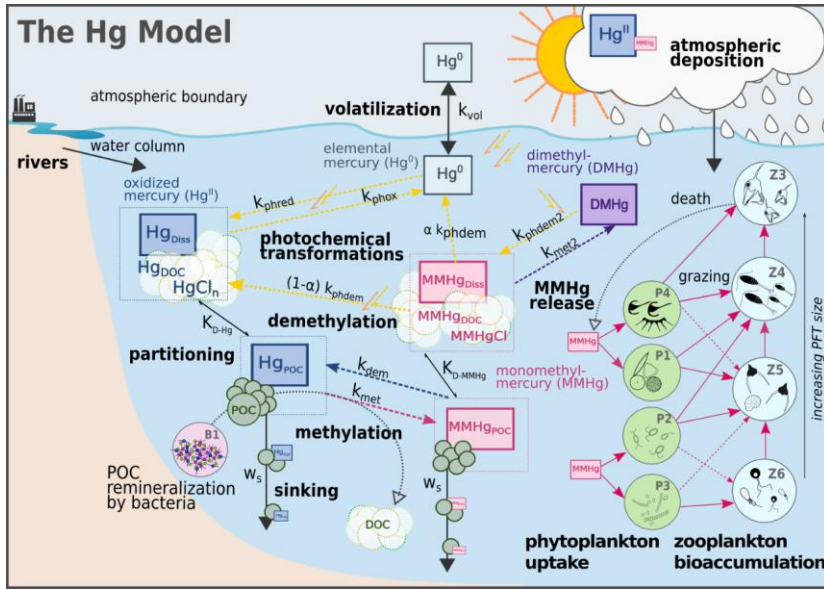


Figure 3: Hg dynamics in the coupled model OGSTM-BFM-Hg. The Hg model simulates the cycling of inorganic ( $Hg^{II}$  and  $Hg^0$ ) and methylated Hg species (MMHg and DMHg) resolving: the partitioning of  $Hg^{II}$  and MMHg between particulate ( $Hg_{POC}$ ,  $MMHg_{POC}$ ) and dissolved species ( $Hg_{Diss}$ , as  $Hg_{DOC} + HgCl_n$ , and  $MMHg_{Diss}$ , as  $MMHg_{DOC} + MMHgCl$ ) based on partition coefficients ( $K_D$ ) and concentrations of POC and DOC, the photochemical and biological transformations (dotted colored arrows) as first order kinetics depending on the rate constants  $k_x$ , the evasion of  $Hg^0$  to the atmosphere controlled by wind speed through the volatilization rate constant  $k_{vol}$ , and the MMHg bioaccumulation (pink arrows) driven by phytoplankton uptake in 4 different PFTs and trophic transfer to 4 zooplankton PFTs.

805

810

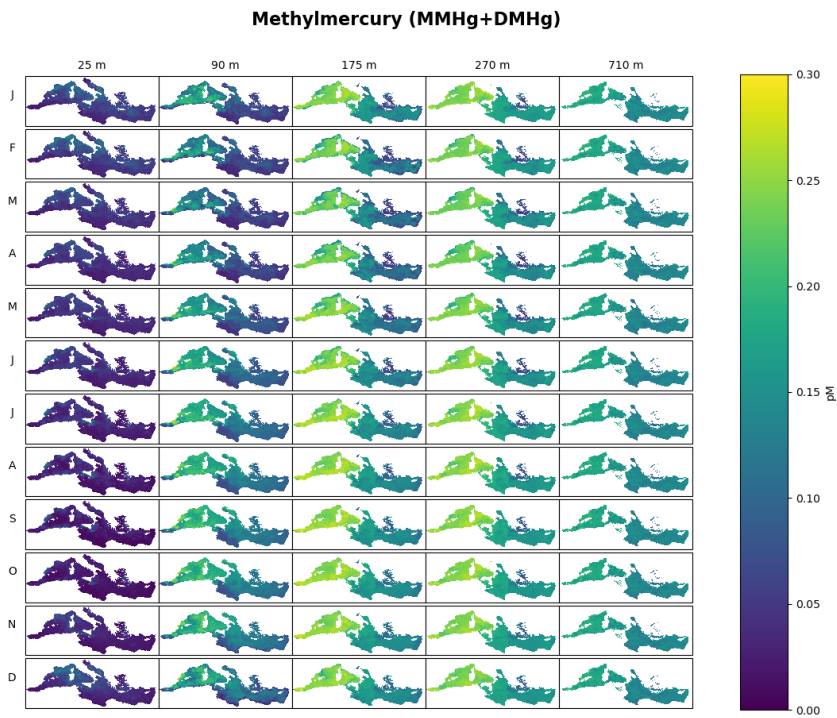
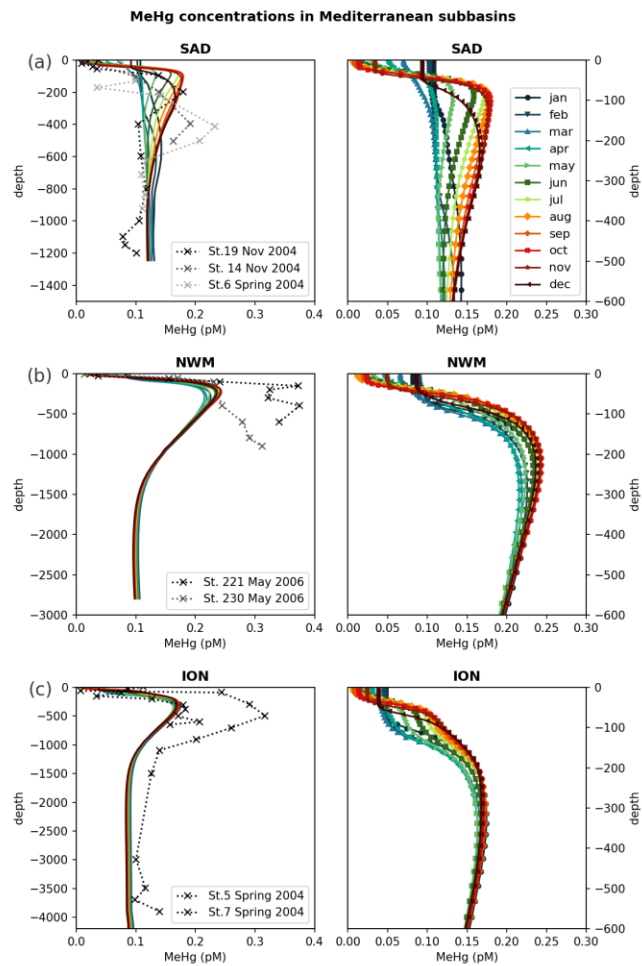


Figure 4: Spatial distribution of monthly averaged MeHg concentrations (pM) in the Mediterranean Sea at different depths in the water column (25, 90, 175, 270 and 710 m-depth) simulated with the OGSTM-BFM-Hg model.



815 **Figure 5:** Vertical profiles of monthly averaged MeHg (MMHg+DMHg) concentrations in the water column reproduced by OGSTM-BFM-Hg model for 2017 (coloured solid lines), compared with observations for 2004-2005 (dotted lines with crosses) available from the literature (Cossa et al., 2009) in three subbasins (Fig. 1): (a) Southern Adriatic Sea (*Sad*), (b) North Western Mediterranean (*Nwm*), and (c) Ionian Sea (*Ion2*). The right panels show the entire water column, and the left panels show a detail of modelled concentrations in the top 600 m of the same subbasins.

ha formattato: Tipo di carattere: Corsivo

ha formattato: Tipo di carattere: Corsivo

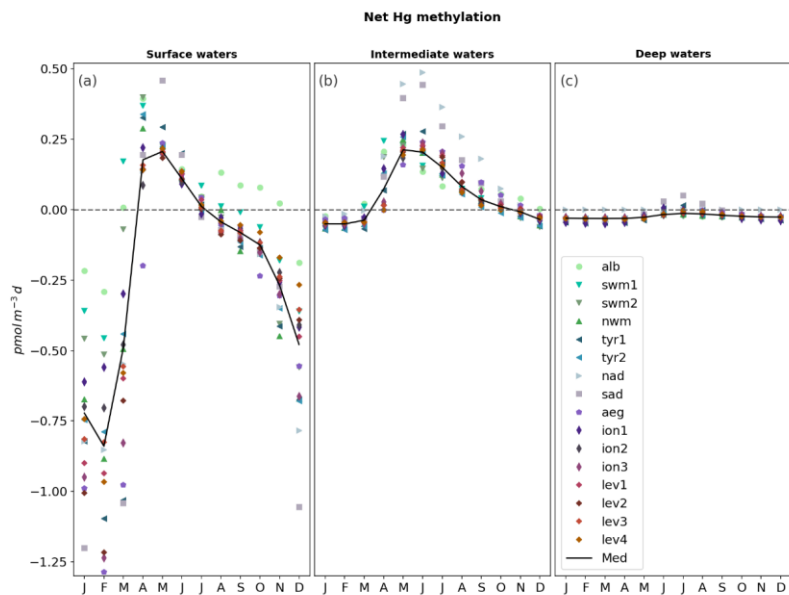


Figure 6: Monthly evolution of the net methylation fluxes ( $\text{pmol m}^{-3} \text{d}^{-1}$ ) for each subbasin (colored markers) of the Mediterranean Sea (black lines) depth-integrated for (a) surface water (0-100 m depth), (b) intermediate water (100-600 m depth), and (c) deep water (>600 m depth). Net methylation is calculated as the difference between modelled Hg methylation fluxes and demethylation fluxes (both dark and photochemical).

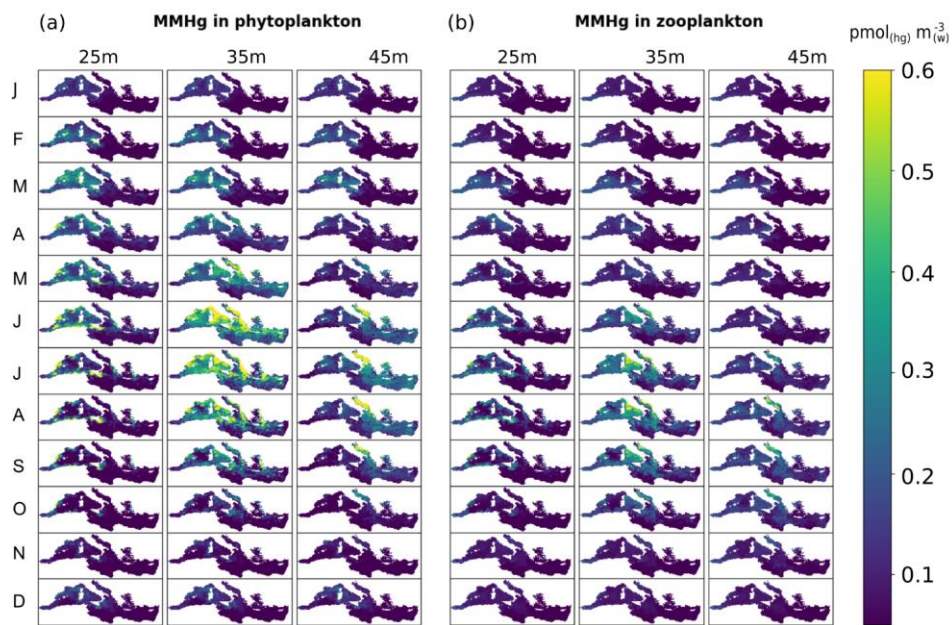
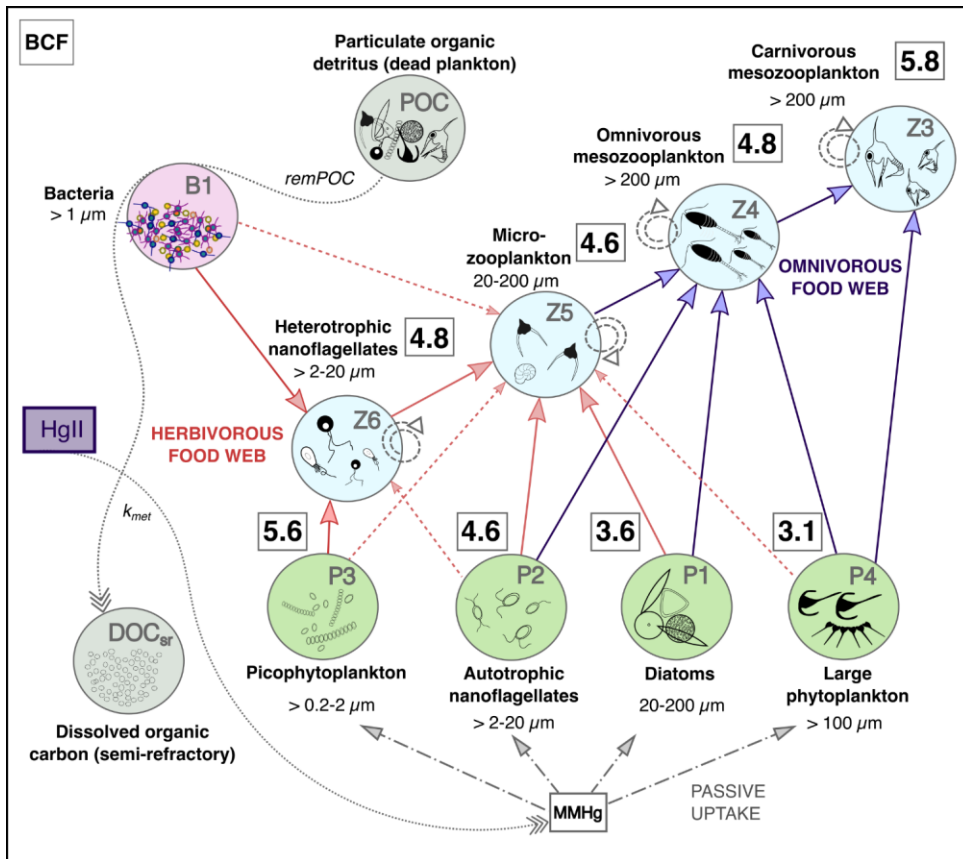


Figure 7: Spatial distribution of monthly averaged (a)  $MMHg_{phy}$  and (b)  $MMHg_{zoo}$  ( $\text{pmol}_{(\text{Hg})} \text{m}_{(\text{w})}^{-3}$ ) in the Mediterranean Sea at different water depths (25 m, 35 m, and 45 m) simulated with the OGSTM-BFM-Hg model for 2017. The plots show the sum of all variables of MMHg in phytoplankton (Fig. S7-S10) and zooplankton (Fig. S11-S14).



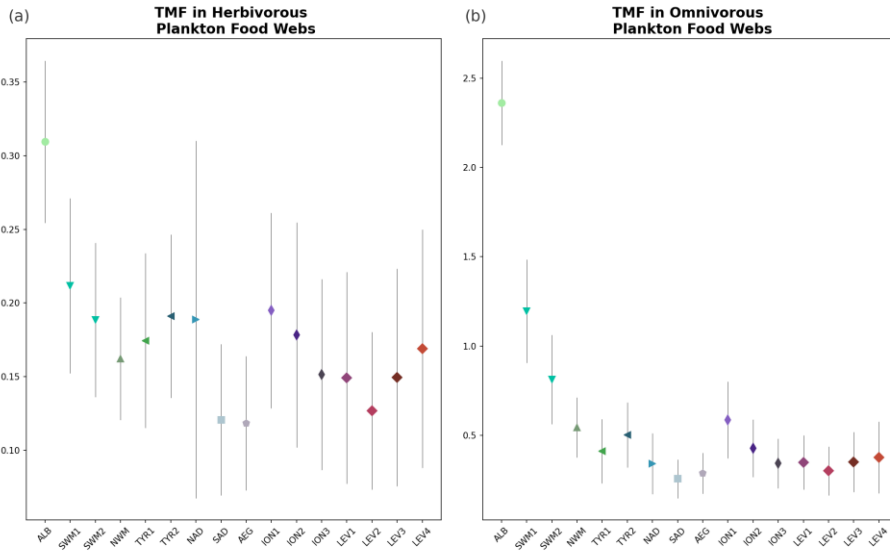


835 Figure 8. Conceptual model of MMHg bioaccumulation in the plankton food web of the OGSTM-BFM-Hg  
 model, subdivided into a lower “herbivorous” (red arrows) and upper “omnivorous” (blue arrows) food webs.  
 The squares with bold numbers show estimated values of Bioconcentration factors ( $\log(\text{BCF})$ ) for each PFT, calculated [for the Sad](#)  
 The squares with bold numbers show estimated values of Bioconcentration factors ( $\log(\text{BCF})$ ) for each PFT, calculated [for the Sad](#)  
 The squares with bold numbers show estimated values of Bioconcentration factors ( $\log(\text{BCF})$ ) for each PFT, calculated [for the Sad](#)  
 840 The squares with bold numbers show estimated values of Bioconcentration factors ( $\log(\text{BCF})$ ) for each PFT, calculated [for the Sad](#)  
 subbasin from spatially averaged model output at monthly resolution. The green circles indicate the four  
 phytoplankton PFTs (P1, P2, P3, P4, representative respectively of diatoms, autotrophic nanoflagellates, picophytoplankton and  
 large phytoplankton), the light blue circles indicate the four zooplankton PFTs (Z3, Z4, Z5, Z6, representative respectively  
 of carnivorous mesozooplankton, omnivorous mesozooplankton, microzooplankton, and heterotrophic nanoflagellates), the purple  
 circle indicate bacteria (B1, representative of all heterotrophic bacteria), and the grey circles indicate particulate organic  
 845 carbon (POC, representative of all organic detritus) and semi-refractory dissolved organic matter (DOC<sub>sr</sub>). The solid arrows show the

ha formattato: Tipo di carattere: Corsivo

850

preferential trophic interactions, the dashed arrows are for secondary trophic interactions (diet switch if the favorite preys are not available), and the circle dashed arrows are for cannibalization within the same zooplankton group. The dash and dotted arrows indicate passive uptake of MMHg by phytoplankton. The dotted arrows indicate the processes of transformation related to carbon recycling by bacteria (remPOC) and of Hg methylation, whose kinetics are coupled through the parameter  $k_{met}$ , converting  $Hg^{II}$  into MMHg.



855 **Figure 9.** Trophic magnification factor (TMF, unitless) for the (a) omnivorous and (b) carnivorous plankton food webs (Figure 8) for each subbasin of the Mediterranean Sea (Figure 3), calculated by integrating over 0-100 m depth the monthly outputs of the OGSTM-BFM-Hg model.

860

Phytoplankton PFTs

		Diatoms	Autotrophic Nanoflagellates	Pico- phytoplankton	Large phytoplankton
$MMHg_{phy, PFT}$	<del>AlbA</del> B	<b>7.1 10<sup>-4</sup></b> (± 5.9 10 <sup>-4</sup> )	<b>5.1 10<sup>-3</sup></b> (± 3.5 10 <sup>-3</sup> )	<b>0.09</b> (±0.05)	<b>1.5 10<sup>-5</sup></b> (± 8.8 10 <sup>-6</sup> )
	<del>SadS</del> D	<b>1.5 10<sup>-3</sup></b> (± 2.7 10 <sup>-3</sup> )	<b>2.6 10<sup>-3</sup></b> (± 3.3 10 <sup>-3</sup> )	<b>0.14</b> (±0.16)	<b>5.1 10<sup>-7</sup></b> (± 6.4 10 <sup>-7</sup> )
$Q_{MMHg, PFT}$	<del>AlbA</del> LB	<b>0.02</b> (± 0.01)	<b>0.15</b> (± 0.09)	<b>1.57</b> (± 1.01)	<b>5.9 10<sup>-3</sup></b> (± 3.7 10 <sup>-3</sup> )
	<del>SadS</del> AD	<b>0.03</b> (± 0.02)	<b>0.27</b> (± 0.22)	<b>2.80</b> (± 2.22)	<b>8.9 10<sup>-3</sup></b> (± 7.2 10 <sup>-3</sup> )
	<del>AlbA</del> LB	<b>3.59</b> (± 0.08)	<b>4.58</b> (± 0.08)	<b>5.59</b> (± 0.07)	<b>3.17</b> (± 0.08)
$\log(BCF_{phy, PFT})$	<del>SadS</del> AD	<b>3.59</b> (± 0.1)	<b>4.60</b> (± 0.08)	<b>5.60</b> (± 0.07)	<b>3.14</b> (± 0.07)
	<b>Zooplankton PFTs</b>				
		<b>Heterotrophic Nanoflagellates</b>	<b>Micro- zooplankton</b>	<b>Onnivorous mesozooplankton</b>	<b>Carnivorous mesozooplankton</b>
$MMHg_{zoo, PFT}$	<del>AlbA</del> LB	<b>9.1 10<sup>-2</sup></b> (± 2.9 10 <sup>-2</sup> )	<b>2.6 10<sup>-2</sup></b> (± 5.1 10 <sup>-3</sup> )	<b>2.1 10<sup>-3</sup></b> (± 5.4 10 <sup>-3</sup> )	<b>1.9 10<sup>-2</sup></b> (± 1.6 10 <sup>-3</sup> )
	<del>SadS</del> AD	<b>7.2 10<sup>-2</sup></b> (± 7.9 10 <sup>-2</sup> )	<b>1.6 10<sup>-2</sup></b> (± 1.7 10 <sup>-2</sup> )	<b>7.1 10<sup>-3</sup></b> (± 7.1 10 <sup>-3</sup> )	<b>1.0 10<sup>-3</sup></b> (± 2.7 10 <sup>-4</sup> )
$Q_{MMHg, PFT}$	<del>AlbA</del> LB	<b>0.39</b> (±0.34)	<b>0.31</b> (±0.29)	<b>0.35</b> (±0.36)	<b>1.04</b> (±0.2)
	<del>SadS</del> AD	<b>0.73</b> (±0.83)	<b>0.42</b> (± 0.55)	<b>0.79</b> (±1.2)	<b>3.60</b> (±2.2)
	<del>AlbA</del> LB	<b>4.90</b> (± 0.17)	<b>4.78</b> (± 0.24)	<b>4.86</b> (± 0.21)	<b>5.50</b> (± 0.29)
$\log(BCF_{zoo, PFT})$	<del>SadS</del> AD	<b>4.80</b> (± 0.36)	<b>4.58</b> (± 0.40)	<b>4.79</b> (± 0.53)	<b>5.81</b> (± 0.36)

Tabella formattata

ha formattato: Inglese (Stati Uniti)

ha formattato: Inglese (Stati Uniti)

ha formattato: Inglese (Stati Uniti)

ha formattato: Inglese (Stati Uniti)

ha formattato: Inglese (Stati Uniti)

ha formattato: Inglese (Stati Uniti)

ha formattato: Inglese (Stati Uniti)

ha formattato: Inglese (Stati Uniti)

ha formattato: Inglese (Stati Uniti)

ha formattato: Inglese (Stati Uniti)

865

**Table 1: Indicators for MMHg bioaccumulation compared for the *Alb* and *Sad* subbasins (Fig. 3). The average ( $\pm$  s.d.) values of the plankton MMHg content ( $MMHg_{PFT}$ ,  $\text{pmol m}^{-3}$ ), the MMHg quota ( $Q_{MMHg,PFT}$ ,  $\text{ng g}_{w.w.}^{-1}$ ), and the bioconcentration factors ( $\log(\text{BCF})$ ) are shown for each phytoplankton and zooplankton PFT.**

**ha formattato:** Tipo di carattere: Corsivo

**ha formattato:** Tipo di carattere: Corsivo